UC San Diego
UC San Diego Electronic Theses and Dissertations

Title

Silicon-rich silicon nitride (SRN) for integrated photonics and thermo-optic applications

Permalink

https://escholarship.org/uc/item/03776806

Author

Nejadriahi, Hani

Publication Date

2022

Peer reviewed|Thesis/dissertation

UNIVERSITY OF CALIFORNIA SAN DIEGO

Silicon-rich silicon nitride (SRN) for integrated photonics and thermo-optic applications

A dissertation submitted in partial satisfaction of the

requirements for the degree Doctor of Philosophy

in

Electrical Engineering (Photonics)

by

Hani Nejadriahi

Committee in charge:

Paul Yu, Co-Chair
Yeshaiahu Fainman, Co-Chair
Prabhakar Bandaru
Zhaowei Liu
Shirley Meng
Steve Pappert

2022

The Dissertation of Hani Nejadriahi is approved and is acceptable in quality and form for publication on microfilm and electronically.

University of California San Diego

2022

DEDICATION

To Mom and Dad, Zahra Pourzanjani and Hossein Riahi

I owe my life to you, and this is just a little thank you for all you have sacrificed for me throughout the years. Your love, support, and encouragements are why I am here today

TABLE OF CONTENTS

LIST OF FIGURES

LIST OF TABLES

ACKNOWLEDGEMENTS

First and foremost, I would like to acknowledge that this work would most certainly not be possible without the guidance of my committee members, help from colleagues, and never-ending support from my family and friends. I am forever grateful.

I would like to express my deepest gratitude to both of my advisors, Prof. Shaya Fainman, and Prof. Paul Yu for hiring me as a graduate student and trusting in me to pursue my research ideas freely. Working with them truly allowed me to become a well-rounded researcher and experience all facets of academia and appreciate the process from bottom to the very top.

I would like to especially thank Dr. Steve Pappert for his continuous guidance during my time at UCSD. He never shied away from sharing his own experiences with me and I have not only learned so much from him academically, but also personally.

I would like to thank Prof. Liu, Prof. Meng, and Prof. Bandaru for agreeing to be on my doctoral committee and for their valuable guidance during my exams and during the course of my studies and research.

I especially want to thank my colleague and husband, Dr. Rajat Sharma, without whom my research would have never flourished. I have learned so much from him throughout the years and am forever grateful that our paths crossed at UCSD. I would also like to thank my amazing colleagues and members of the Fainman and Yu group especially Alex Friedman, Prabhav Gaur, Chengkuan Gao, Karl Johnson, and Andrew Grieco, who were always helpful in my research and my life and allowed the research environment to be extremely friendly and positive.

Finally, I would like to thank my parents, my sisters, Halleh, Hasti, my brother, Hami and their lovely families for their constant love and support. They have always been there for me during my toughest times and encouraged me to be the best version of myself. After long hours in

the lab, being able to see my family and spend time with them was probably the number one source of my happiness and comfort.

Chapter 2, in part, contains materials from "Thermo-optic properties of silicon-rich silicon nitride for thermo-optic applications", published in Optics Express. This paper was co-authored by Alex Friedman, Rajat Sharma, Steve Pappert, Yeshaiahu Fainman, and Paul Yu. The dissertation author was the first author of the manuscript.

Chapter 3, in part, contains materials from ""Efficient and compact thermo-optic phase shifter in silicon-rich silicon nitride", published in Optics Letters and also "Compact, high efficiency thermo-optic switch realized using silicon-rich silicon nitride", submitted for publication. Both of these papers were co-authored by Steve Pappert, Yeshaiahu Fainman, and Paul Yu. The dissertation author was the first author of the manuscript.

Chapter 4, in part, contains materials from "Wide-angle optical beam steering in SRN" submitted for publication in Optics Letters and co-authored by Prabhav Gaur, Alex Friedman, Karl Johnson, Steve Pappert, Yeshaiahu Fainman, and Paul Yu. The dissertaion author was the first author of the manuscript.

Chapter 5, in part, contains materials from "Wide-angle optical beam steering in SRN" submitted for publication in Optics Letters and co-authored by Prabhav Gaur, Alex Friedman, Karl Johnson, Steve Pappert, Yeshaiahu Fainman, and Paul Yu. The dissertaion author was the first author of the manuscript.

2014	Bachelor of Arts in Math, Physics, and Music, Saint Olaf College, Northfield, MN
2017	Master of Science in Electrical Engineering (Photonics), The George Washington University, Washington, D.C.
2022	Doctor of Philosophy in Electrical Engineering (Photonics), University of California San Diego, USA

JOURNAL PUBLICATIONS

- **Hani Nejadriahi,** Alex Friedman, Rajat Sharma, Steve Pappert, Yeshaiahu Fainman, and Paul Yu, "Thermo-optic properties of silicon-rich silicon nitride for on-chip applications," Opt. Express 28, 24951-24960 (2020)

- **Hani Nejadriahi,** Steve Pappert, Yeshaiahu Fainman, and Paul Yu, "Efficient and compact thermo-optic phase shifter in silicon-rich silicon nitride," Opt. Lett. 46, 4646-4649 (2021)

- **Hani Nejadriahi**, Steve Pappert, Yeshaiahu Fainman, and Paul Yu, "Compact, high efficiency thermo-optic switch realized using silicon-rich silicon nitride," JLT (In preparation for submission)

- **Hani Nejadriahi**, Prabhav, Gaur, Alex Friedman, Karl Johnson, Steve Pappert, Yeshaiahu Fainman, Paul Yu, "Sub-wavelength-pitch silicon-rich silicon nitride optical phased array for one dimensional beam steering," Optica (In preparation for submission)

- Alex Friedman, **Hani Nejadriahi**, Rajat Sharma, and Yeshaiahu Fainman, "Electro-Optic Switching in Silicon-Rich Nitride," in OSA Nonlinear Optics 2021, R. Boyd, C. Conti, D. Christodoulides, and P. Rakich, eds., OSA Technical Digest (Optical Society of America, 2021), paper NW2B.3.

- Li-Yang Sunny Chang, **Hani Nejadriahi**, Steve Pappert, and Paul K. L. Yu, "Demonstration of DC Kerr effect induced high nonlinear susceptibility in silicon rich amorphous silicon carbide", Appl. Phys. Lett. 120, 071107 (2022).

ABSTRACT OF THE DISSERTATION

Silicon rich silicon nitride (SRN) for integrated photonics and thermo-optic applications

by

Hani Nejadriahi

Doctor of Philosophy in Electrical Engineering (Photonics)

University of California San Diego, 2022

Professor Paul Yu, Co-Chair

Professor Yeshaiahu Fainman, Co-Chair

It is important to note that current LIDAR systems rely on rotating the device to scan the field of view in one dimension. Although mechanical rotations allow for a full 360 degrees scan, it requires bulky apparatus that are not so robust to vibrations and harsh environments. Thus, the need for compact, low cost and small-scale solid-state LIDAR is evermore increasing.

Silicon photonics seems to be a viable solution for the future of on-chip communication. The advancements in silicon photonics, and CMOS compatible foundries, allow for the fabrication of the next generation of miniaturized optical components and photonic integrated circuits i.e., phased arrays. Silicon

photonics has been at the forefront of optical communications and the next generation of optical transceivers. As a result, there has been also some development in the optical phased arrays.

Phased arrays are antenna-based devices whereby controlling the phase and amplitude of each individual antenna and due to the interference between them, one can generate an arbitrary emitted pattern. Radio frequency based phased arrays have long been in use for decades and are a big part of data communication. They are considered the "de facto" way to do solid-state electronic beam steering for many RADAR systems. However, devices used for the optical phased arrays offer high pointing accuracy and resolution in a smaller size compared to the radio frequency counterparts due to the much shorter wavelength of light.

Despite its immense potentials optical phased arrays have yet to become a commercial product. Part of the reason for that has been the lack of an ideal platform. Existing optical phased arrays are mostly based on silicon and stoichiometric silicon nitride. Although they can each be useful for specific applications however, they have some drawbacks. First, stoichiometric silicon nitride due to its lower index and thermo-optic coefficient at the telecom wavelengths, lacks an efficient phase tuning mechanism. Additionally, the waveguiding structure needs to be larger to have a more confined optical mode which makes the footprint and scaling in the system challenging issues.

On another note, silicon based optical phased arrays are not ideal for high-power operation. Due to the losses in the system and the presence of grating lobes, the system requires a greater amount of input power to achieve a given output power. However, this also increases the chance of damage at the input (due to nonlinear optical losses), where the power is the highest. This is due to the high two/multi-photon absorption coefficient present in silicon.

As such, we are proposing a new platform with our high index plasma-enhanced chemical vapor deposited (PECVD) silicon-rich silicon nitride where the positive attributes of both silicon and stoichiometric silicon nitride are combined.

The objective of this thesis is to provide a systematic approach towards the development of a novel CMOS compatible platform (high index silicon-rich silicon nitride) which can be an ideal alternative to the existing platform used for OPAs utilizing the thermo-optic effect.

We provide a systematic approach towards the development and the enhancement of PECVD deposited silicon nitride's thermo-optic coefficient as a function the deposition parameters and the silicon content. The ratio of the Si/N is adjusted by changing the ratio of the precursor gases used during the deposition (SiH_4/N_2). We achieve a wide range of linear refractive indices (1.92-3.1 measured at $\lambda = 1550$ nm). We show that highly silicon-rich silicon nitride (SRN) films with index n>3 possess a much larger transparency window extending to the telecom wavelengths while maintaining low loss optical waveguiding in the C-band.

We further show that thermo-optic coefficient of our highest index nitride film with n = 3.1 is (1.65 x 10^{-4} K^{-1}) which is very close to that of crystalline silicon.

We then utilized this high index SRN film with a high thermo-optic coefficient to design, fabricate, and characterize photonic integrated circuits that could potentially be used for a phased array system. The cascaded and compact splitters: y-branch and multi-mode interference coupler for splitting the laser beam onto the chip, multimode interferometric switch for amplitude control, thermo-optic phase shifter for phase tuning the antennas, compact bends in single and multi-mode waveguides implemented in the switch and the phase shifter, and the effective index mismatched closely spaced waveguides for creating a phase difference between them to avoid coupling in the near-field (even when their evanescent fields overlap).

Finally, we were able to fully integrate and experimentally demonstrate an SRN based end-fire facet optical phased array with 16 elements at $\frac{\lambda}{2}$ spacing (775 nm) that has a spot size of about 6 degrees at boresight (0 degrees). The wide steering range is close to a full 120 degrees with one dimensional field of view. The high beam quality in our system is due to a) our compact and efficient phase shifter design which allows for localized heating with negligible crosstalk, b) along with the phase mismatched for the closely spaced waveguides antennas. Such system can be scaled and used for the next generation of LiDAR applications.

CHAPTER 1

INTRODUCTION

Depending on the application, designing silicon photonics phased array-LIDAR requires many system-specific considerations; the most important of which is the waveguiding material. Most silicon photonics products are fabricated using the popular silicon-on-insulator (SOI) wafers. Silicon is the workhorse of CMOS industry, and its SOI implementation is used commonly with a device layer of 220 nm although some variations exist depending on the application and for more tolerable optical performance. Because of its many advantages such as high index contrast with the oxide cladding (allows for creation of compact structures), high thermo-optic coefficient (for efficient phase shifting/modulation and fast tuning speed), transparency in the O and C-bands which makes it attractive for a range of optical processing application.

However other materials such as silicon nitride, commonly used in foundries as a centrosymmetric, CMOS compatible platform. It can also be used as the device layer's core material. Silicon nitride is another versatile material which is generally deposited using chemical vapor depositions. From the standpoint of integrated photonics, silicon nitride has many advantages such as low loss waveguides, larger transparency window (extending to beyond the visible wavelengths), high power handling capability on account of low two-photon-absorption (TPA) losses, ease of tuning and deposition. However, despite so many advantages that both silicon and silicon nitride offer, they have their shortcomings too.

Silicon lacks a wide transparency window due to its bandgap ~ 1.1 μm and thus cannot be used for a wider range of applications. Additionally due to the presence of TPA, this nonlinear phenomenon limits the power handling capabilities of silicon which is a major drawback for optical phased arrays. Although

silicon as a semiconductor can be used for doped waveguide heaters, they can introduce even more optical loss in the system due to the free carrier absorption (FCA) and their large footprints.

Stoichiometric silicon nitride also on accounts of its low refractive index and thermo-optic coefficient is not necessarily the best platform for a scalable and efficient phased array lidar system.

Focusing however on the benefits of both silicon and silicon nitride, there is another CMOS compatible material with a lot of potential in integrated photonics. Increasingly researchers have shown that by tuning and increasing the silicon content in silicon nitride thin films, nonlinear coefficient (third-order nonlinear susceptibility $\chi^{(3)}$ can also be tuned up to 4-5 times higher than that of crystalline silicon. This is while the material contains a larger transparency window compared to silicon and low TPA similar to that offered by stoichiometric silicon nitride. Hence, it is considered viable candidate for on-chip applications.

Table 1.1. below shows a summary comparison of the properties of the three materials.

Table 1.1. Comparison of the different material platforms

Material platform	Index @ 1550 (nm)	Transparency Window (μm)	Bandgap (eV)	Thermo-optic Coefficient	β_{TPA} (cm/GW)	n_2 (m^2/W)
Si$_3$N$_4$	1.98	0.25-8	5	2×10^{-5}	Negligible	2.4×10^{-19}
Si	3.437	1.1-9	1.12	1.84×10^{-4}	0.5	2.5×10^{-18}
SRN	2.1-~3.14	0.72-8	3	**1.65×10^{-4}**	Negligible	2.8×10^{-17}

It is noteworthy that one of the key drawbacks with SRN is the increased linear absorption at the telecom wavelength due to the presence of the silicon nanoclusters. This is usually due to the presence of ammonia, NH$_3$ in deposition which leads to the creation of N-H bonds. This problem usually gets worse when rapid thermal annealing is used to passivate these bonds. High temperature annealing forms silicon nanoclusters which are the result of out-diffusion from the substrate.

In our approach, we investigate a different way towards the deposition of low temperature PECVD SRN with no ammonia used in the recipe. We further show that by just using SiH_4 and N_2 gases we can accurately tune the index of our films while maintaining low loss and a large transparency window (~ 700 nm-1600 nm measured) using the ellipsometry techniques.

We also report the highest measured thermo-optic coefficient for a PECVD deposited SRN film. We do so for different compositions of our silicon nitride films from stoichiometric silicon nitride all the way to the ammonia free silicon rich silicon nitride.

Hence, we believe our high index, low loss and high thermo-optic coefficient SRN films can offer a promising complementary platform to the existing silicon and silicon nitride OPAs. We show a 16-element one dimensional phased array on-chip circuit wore-bonded to a PCB for the phase control. This optical phased array is based on an end-fire facet design with compact phase shifters, multi-mode interference coupler splitters, and phase mismatched waveguides as the arraying antenna. We report a 6.5° spot size at bore-size and a steering range of 115°.

In this thesis, we undertake a systematic approach towards developing the SRN films while enhancing their linear refractive index and thermo-optic coefficients, engineering photonics components, and finally integrating them towards a full optical phased array system.

Chapter 2 describes the systematic study on the effect of increasing the silicon content in the nitride films on their exhibited thermo-optic properties. In order to do so, we carried out thermo-optic measurements using Mach Zehnder interferometers (MZIs) fabricated with nitride films over a wide range of indices: 1.92 (silicon deficient films) – 3.1 (silicon-rich films). We conclusively demonstrate that increasing the silicon content leads to an increase in the films' thermo-optic coefficients, with highly silicon-rich films (n = 3.1) exhibiting a thermo-optic coefficient comparable to that of silicon. We further demonstrate that such films, despite their high silicon content, retain low optical loss over a much wider

range of wavelengths than that of silicon and can indeed be used for low loss waveguiding in the NIR regime.

Chapter 3 describes the design, fabrication, and characterization of the components needed for the integration of the 16-element phased array. First different splitter designs were studied and explored. Here the y-splitter and the MMI coupler designs are explored. Then for the amplitude control on the OPA chip two different MMI switches are studied and experimentally demonstrated. First a straight design and second by implementing the modified Euler bends, the effects on the performance properties are discussed. These bends structures are studied for both single and multi-mode waveguides. To provide the phase shifting, we show the experimental verification of single mode modified Euler bends used in the compact and efficient design of the phase shifters with compact heater geometries. Lastly the phase mismatched waveguides used for the end-fire facet design of the waveguide antennas are discussed and experimental results are shown.

Chapter 4 describes the current research in optical phased array and LIDAR technology. Followed by the mathematics of antenna arrays in general along with some theoretical models of our phased array design. We demonstrate the FDTD simulation of the end-fire facet design of the OPA and finalize our antenna design. Finally, we show the final OPA chip design and its layout.

Chapter 5 describes the cascaded architecture used in our array design along with some finite difference time domain (FDTD) simulations of the phased array design. Further, the design of the PCB along with limitation and challenges are discussed. To control the phase shifters implemented in the phased array a microcontroller is used to connect to the PCB and actively tune the heaters. Finally, the experimental measurements of the phased array along with the optical setup used to get the results are discussed. Chapter 6 summarizes the research contributions of this dissertation and proposes possible future research directions.

Chapter 2

Thermo-optic properties of silicon-rich silicon nitride

2.1 Background

Presently, increasing the silicon content in silicon nitride thin films is being investigated towards creating a material platform that combines the benefits of silicon and stoichiometric silicon nitride. It has been shown that silicon-rich silicon nitride (SRN) films can demonstrate a highly enhanced nonlinear coefficient (third-order nonlinear susceptibility χ (3) up to 4-5 times higher than that of crystalline silicon) while retaining low two-photon absorption (TPA) a in the Near Infra-Red (NIR) like stoichiometric nitride and a larger transparency window than that offered by crystalline silicon [1,2]. As such, it is a viable candidate for on-chip applications such a super-continuum generation, wave-mixing, signal processing and light detection and ranging (LIDAR) [3,4]. The enhancement in SRN's nonlinear coefficient has commonly been attributed in the literature to its higher silicon content and in particular the presence of embedded silicon nanocrystals [5]. There has also been some discussion in literature on the possible enhancement of thermo-optic properties of silicon nitride as a function of its silicon content [6]. The thermo-optic coefficient of stoichiometric silicon nitride is commonly exploited for realizing on-chip devices such as electro-optic phase shifters [7] for various applications. However, on account of its low thermo-optic coefficient (2.45×10^{-5} K^{-1}) [8] and low refractive index, these devices suffer from low device efficiency in terms of high electrical power consumption and large device footprint [3,7]. Silicon on the other hand possesses a higher thermo-optic coefficient (1.86×10^{-4} K^{-1}) but suffers from a much narrower transparency window (transparent beyond 1.1 µm) and lower optical power handling capability on account of loss mechanisms such as two photon absorption (TPA) and surface carrier absorption (SCA) [5,9–10].

In this work, we present SRN as an alternative material for on-chip applications that utilizes the thermo-optic effect. We provide a systematic evaluation of enhancement of PECVD deposited silicon

nitride's thermo-optic coefficient as a function of its silicon content. Using this method, we conclusively demonstrate that the Si/N ratio of silicon nitride films can be adjusted by tuning the ratio of the precursor gases (SiH_4/N_2) in the PECVD system achieving films with a wide range of linear indices (1.92- 3.1, measured at $\lambda = 1550$ nm). We demonstrate that highly silicon-rich silicon nitride films (refractive index, n > 3) possess a much wider transparency window than that of silicon and can be used to demonstrate low loss optical waveguiding in the C-band. We then characterize the thermo-optic response of MZIs fabricated with silicon nitride films of different compositions and quantitatively demonstrate an enhancement in the thermo-optic coefficient as a function of silicon content in these films.

2.2 Film Preparations and optical properties

In the current work, PECVD was employed to deposit silicon nitride films of varying composition on top of oxide-on-silicon substrates. Deposition of silicon nitride using PECVD offers an advantage in terms of lower deposition temperature (350 °C in this study), as compared to LPCVD which is carried out at high temperatures (in the range of 700-800 °C). The ratio of precursor gases, SiH_4, N_2, and NH_3 was then varied, as shown in Table 2.1., to realize three samples, S1, S2, and S3. For the purposes of ellipsometry measurements we maintained a film thickness of < 100 nm for all the three films. The Energy Dispersive Spectrum (EDS) measurements carried out in our previous work [11] and other works in literature [5,12] have clearly demonstrated that increase in the linear refractive index of the deposited CVD silicon nitride films is accompanied by an increase in their silicon content. Ellipsometry measurements were then carried out to determine the real and imaginary parts of the linear refractive index of these films with the latter defining their transparency windows. Table 2.1. shows the real part of the refractive index measured at 1550 nm for films S_1 through S_3 confirming that linear refractive index increases with increase in silicon content in silicon nitride films. Fig. 2.1. shows the dispersion in the real and imaginary part of the refractive index for sample S3 over a wide wavelength range, 200-1600 nm. It is clearly visible that the imaginary

6

part of the index, and hence the optical loss, of the film remains negligible even at wavelengths as low as 700 nm despite it having a silicon content significantly higher than that of stoichiometric silicon nitride. This also demonstrates that PECVD can be used to deposit highly silicon-rich silicon nitride films of index greater than 3 with low optical loss and wide transparency windows. Further, the inset in Fig. 2.1 demonstrates how the refractive index of SRN films can be tuned as a function of the SiH_4/N_2 ratio in ammonia free recipes.
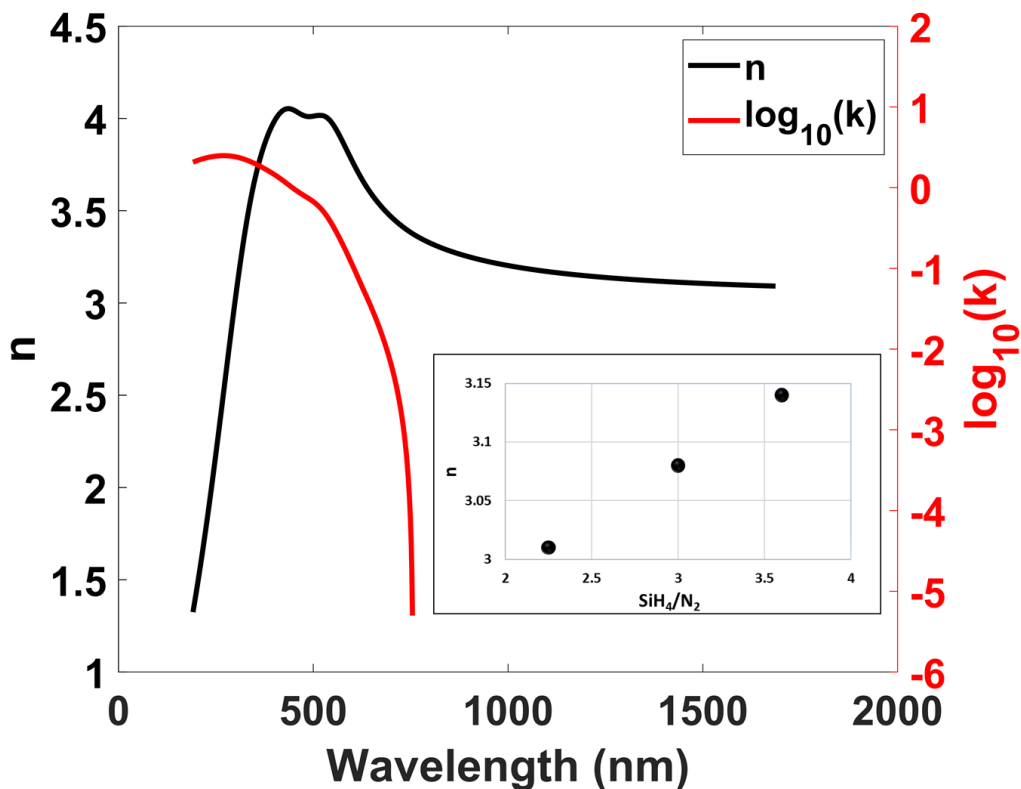
Figure 2.1. Ellipsometry measurements for sample S3 with n = 3.1 at λ=1550 nm showing the real (in black) and log of the imaginary part (in red) of the refractive index. It should be noted that the accuracy of the ellipsometer in the measurement of the imaginary part of the refractive index is limited to 10−5 which occurred at a wavelength of about 755 nm, leading to the abrupt stop in the plot of log10(k) versus wavelength; the inset shows the enhancement of the index of SRN films for the ammonia free condition with refractive indices of 3.01, 3.08, and 3.11.

Table 2.1. Deposition parameters and the refractive index of silicon nitride with various compositions with thickness of 60 nm

Sample #	n (λ=1550 nm)	SiH$_4$ Flow Rate (sccm)	N$_2$ Flow Rate (sccm)	NH$_3$ flow rate (sccm)
S1	1.92	276	600	24
S2	2.25	400	200	10
S3	3.1	500	150	0

2.3 Loss Characterization for SRN waveguides

While the ellipsometry measurements show that SRN films with linear refractive indices higher than 3 are indeed low loss in the NIR region (O and C bands), it is still important to evaluate their loss by in waveguide propagation. For this purpose, we carried out the fabrication of bus-coupled ring resonators (i.e., all pass filter) with a range of coupling gaps using our PECVD deposited SRN films with n = 3.1 (measured at λ = 1550 nm). Starting with a wafer with 3 μm of thermal oxide on top of a silicon substrate, we first deposited a 320 nm thick SRN film using the recipe for the film sample S$_3$ (see Table 2.1). Bus-coupled ring resonators with waveguide widths of 400 nm and ring radius of 45 μm are then fabricated using E-beam lithography followed by dry-etching using a C$_4$F$_8$ and SF$_6$ plasma in an Oxford Plasmalab 100 etcher which is the typical recipe used in [13]. The gas flow rates during the etching process were 25 sccm for SF$_6$ and 50 sccm for C$_4$F$_8$, and the chamber pressure was maintained at 15 mTorr. The device fabrication is then completed with a deposition of 2 μm PECVD silicon dioxide as top clad followed by a 15-minute rapid thermal anneal (RTA) in a forming gas H$_2$/N$_2$ (10%:90%) ambient. The transmission response of these ring-resonators was then measured in the C-band using a tunable CW Agilent laser and a fiber-in, free-space out setup such as that presented in our previous work [13]. Fig. 2.2(a) and (b) show the measured response with a zoom-in of a single resonance and multiple resonances respectively for an SRN

ring resonator with a 140 nm coupling gap for a propagating TM-polarized optical mode. The free-spectral

range (FSR) measured using this response is 2.381nm, corresponding to a group index of 3.58, which in

turn is very close to the value predicted using eigenmode analysis in Lumerical MODE with the same

waveguide dimensions and measured refractive index. Fig. 2.2(a) also shows a single resonance from the

response fit to a well-known Lorentzian expression [14] for the transmission response of a bus-coupled ring

resonator which is then used to estimate the loss of the propagating mode. The optical loss coefficients

extracted for the TE- and TM-like optical modes using this methodology are 7 dB/cm and 3.27 dB/cm

respectively similar to those reported in [12,15–16]. These loss values are comparable to those obtained for

deposited amorphous silicon waveguides [17] but higher than those usually observed for state-of-the-art

silicon and silicon nitride waveguides [3,18]. However, it should be noted that this loss can be attributed to

a combination of an unoptimized fabrication process and/or possible material losses resulting from the

inherent nature of high-index SRN films themselves [11,18–20]. The combination of low optical loss and

high refractive index would allow for the design of multi-mode straight and bent waveguides with

comparable dimensions to those made using crystalline silicon [21].
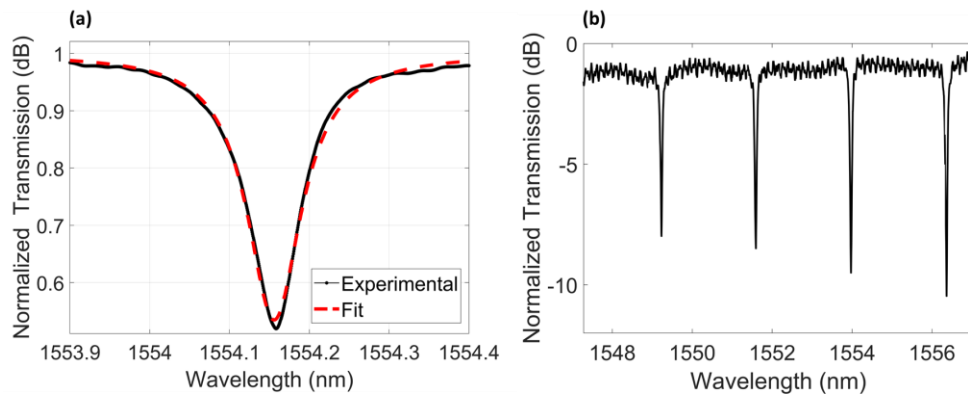
Figure 2.2. Passive transmission spectra for a ring resonator, corresponding to a 140 nm coupling gap and TM polarization for the optical mode (a) Single resonance at 1554.15 nm overlayed with the Lorentzian fit for the transmission response of a ring resonator (b) multiple resonances for the same ring resonator

2.4 Thermo-optic characterization for SRN waveguides

In order to determine the effect of silicon content on the thermo-optic response of the silicon nitride films, we fabricated three different sets of MZIs (S_1, S_2, and S_3) using the three different films prepared following the deposition procedures described in section 2. Figure 2.3(a) shows an optical microscope (OM) image of one of the fabricated MZI sets with integrated heater filaments and contact pads. Figure 2.3(b) is a cross-sectional schematic of the device, showing the Ni:Cr heating filaments fabricated using a combination of photolithography (bilayer photoresist consisting of PMGI and AZ1512 and mask-less aligner Heidelberg 150) and RF sputtering (Denton 635). The dimensions of the heater filaments in each MZI set were 300 nm in height, 20 μm in width, and four different lengths of 480, 980, 1480, and 1980 μm as shown in Fig. 2.3(a). On account of the high variation in the nitride film refractive indices, $n_{S1} = 1.92$, $n_{S2} = 2.25$, $n_{S3} = 3.1$, different film thicknesses and waveguide widths were chosen to ensure high overlap of the optical mode with the waveguide core. The waveguide dimensions for the three cases are listed in Table 2.2. Fig. 2.3(c) shows an SEM micrograph of a Y-splitter at the input end of one of the MZIs. It should be noted that while heater filaments were placed on both arms of the MZI, to balance the optical loss, one of the arms was left disconnected from the contact pads.

Table 2.2. Performance parameters of the MZI with 3 SiNx recipes for measuring thermo-optic coefficient

Sample #	$w \times h$ (nm^2)	Γ_{SiNx}	FSR (nm)	n_g	$\Delta n/\Delta T$ (K^{-1})
S1	800×550	59%	11.5	1.84	$(1.82 \pm 0.8) \times 10^{-5}$
S2	600×400	57%	8.96	2.39	$(5.85 \pm 0.5) \times 10^{-5}$
S3	400×320	69%	5.94	3.96	$(1.65 \pm 0.08) \times 10^{-4}$

To extract the thermo-optic coefficients of the three films, we then measured the spectral response of the shortest MZIs as a function of power in the heaters for all the three sets. Doing so allowed us to determine the change in the effective refractive index and hence the change in the material index of the

waveguide core as a function of temperature. This step was performed by combining our experimental results with eigenmode and thermal modeling in Lumerical MODE and Lumerical DEVICE respectively.
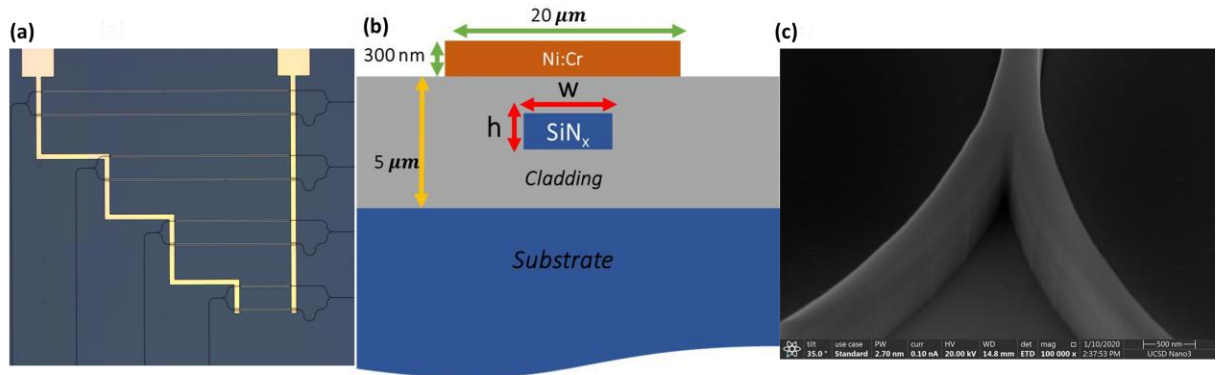
Figure 2.3. (a) OM top view of the four MZIs with integrated Ni:Cr heaters and Cr/Au contact pads consisting of 680 to 1920 µm of balanced lengths and 102 µm of imbalanced length (b) schematic of the SiNx based MZIs with waveguide dimensions of h and w listed in Table 2.2. and total cladding thickness of 5 µm along with Ni:Cr heater filament of 20 µm width and 300 nm height (c) SEM image of the Y junction at the output port of the fabricated MZI

Transmission spectral scan were taken as a function of voltage applied to the heater. Fig 2.4(a) shows the experimentally measured spectral response of the shortest MZI in sample S3 for a voltage range of 0 to 6 V. Fig. 2.4(b) shows the extracted spectral shift $\Delta\lambda$, (in black) in the MZIs transmission response as a function of voltage applied. Also shown in the same figure (in red) is the experimentally measured power consumed in the heater. As shown, the spectral shift is a quadratic function of the voltage applied. This is because the power dissipated by the heater (P) is a quadratic function of the voltage applied ($P = \frac{V^2}{R}$), where R is the resistance of the heater element, and is linearly proportional to the change in temperature in the waveguide core (ΔT). This was confirmed using thermal simulations carried out in Lumerical DEVICE. [8]. Equation (1) describes the relationship between the experimentally observed $\Delta\lambda$ and the thermo-optically induced change in the effective index (Δn_{eff}) of the optical mode. Here λ_{null} is the wavelength corresponding to the null point in transmission, ng is the group index calculated from the measured free spectral range (FSR) [14], L_{mod} is the heater length of 480 µm, and $\Delta L = 102$ µm is the imbalanced length.

$$\left(\frac{\Delta n_{eff}}{n_g}\right)\left(\frac{L_{mod}}{\Delta L}\right) = \frac{\Delta\lambda}{\lambda_{null}} \qquad (1)$$

11

Hence knowing the spectral shift $\Delta\lambda$ as a function of change in temperature of the waveguide core (ΔT), we can use Eq. (1) to calculate Δn_{eff} as a function of ΔT shown in Fig. 2.4(c) for the three films. This change in effective index as a function of temperature, can then be related to the change in material indices via Eq. (2) where $\left(\frac{\partial n}{\partial T}\right)_{SiO_2} = 9 \times 10^{-6} K^{-1}$ [22,23] and $\left(\frac{\partial n}{\partial T}\right)_{SiNx}$ are the thermo-optic coefficients for the cladding oxide (as reported in literature) and silicon nitride respectively, and Γ_{SiNx} and Γ_{SiO_2} are the overlap factors of the mode with the silicon nitride waveguide core and the cladding oxide respectively. The overlap factor, Γ, in this equation is calculated in a manner similar to that reported in ref. [24,25].

$$\frac{\Delta n_{eff}}{\Delta T} = \Gamma_{SiO_2} \left(\frac{\partial n}{\partial T}\right)_{SiO_2} + \Gamma_{SiNx} \left(\frac{\partial n}{\partial T}\right)_{SiNx} \tag{2}$$

The calculated values of the overlap factors within the waveguide cores are shown in Table 2.2. below. Using these confinement factors, the $\Delta n/\Delta T$ for all three films was obtained. Thermo-optic coefficient extracted was determined to be $(1.65\pm0.08) \times 10^{-4}$ K^{-1} for S_3, $(5.85\pm0.5) \times 10^{-5}$ K^{-1} for S_2, and $(1.82\pm0.8) \times 10^{-5}$ K^{-1} for S_1. The uncertainties in the coefficients arise from an uncertainty in both post-etch waveguide dimensions as well as that in the shape and thickness of the deposited top cladding PECVD oxide. The enhancement of the coefficient can be seen in the plot below as a function of the measured refractive index values for each of them. The result clearly shows the enhancement as a function of increase in the silicon content of the silicon nitride films with the highest achieved thermo-optic coefficient being comparable to that of crystalline silicon [26].
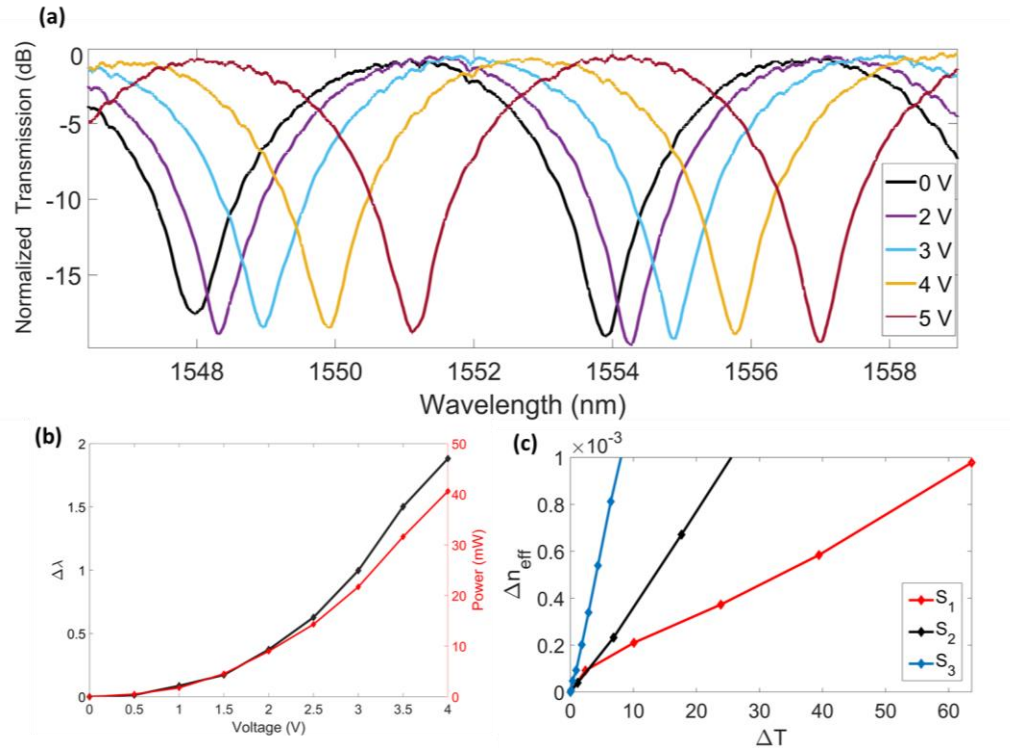
Figure 2.4. (a) Spectral shift of the null point in transmission due to the applied voltage for sample S3 (b) relative change in the wavelength and the power increase in the heater as functions of the applied voltage to the heater corresponding to (a), (c) the effective index change obtained from Eq. (1) for MZIs of all the three sets
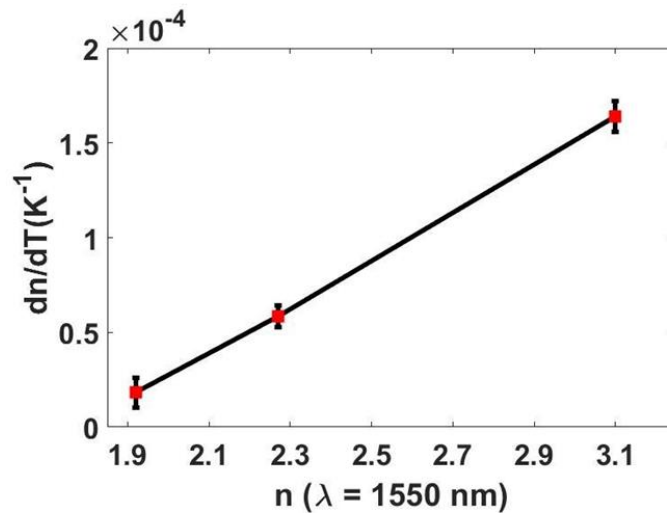
Figure 2.5. Enhancement of the thermo-optic coefficient and its relation to the refractive index with the corresponding uncertainties at $\lambda = 1550$ nm

2.5 CONCLUSION

In conclusion, we report experimental data on the thermo optic coefficient of PECVD deposited silicon nitride films, achieving a value as high as $(1.65\pm0.08) \times 10^{-4}$ K $^{-1}$ for a film with refractive index of 3.1. This is one of the highest reported thermo-optic coefficients in a PECVD deposited silicon nitride film to date and is comparable to that of crystalline silicon [32]. As expected, a clear correlation is experimentally demonstrated between the silicon concentration of the deposited silicon nitride films and their corresponding thermo-optic coefficients. We also demonstrate that these nitride films retain low optical loss, even at indices greater than 3.

Chapter 2, in part, contains materials from "Thermo-optic properties of silicon-rich silicon nitride for thermo-optic applications", published in Optics Express. This paper was co-authored by Alex Friedman, Rajat Sharma, Steve Pappert, Yeshaiahu Fainman, and Paul Yu. The dissertation author was the first author of the manuscript.

Bibliography

Chapter 2

1. D.T.H. Tan, K.J.A. Ooi, and D.K.T. Ng, "Nonlinear optics on silicon-rich nitride—a high nonlinear figure of merit CMOS platform," Photonics Res. 6(5), B50–B66 (2018).

2. K. J. A. Ooi, D. K. T. Ng, T. Wang, A. K. L. Chee, S. K. Ng, Q. Wang, L. K. Ang, A. M. Agarwal, L. C. Kimerling, and D. T. H. Tan, "Pushing the limits of CMOS optical parametric amplifiers with USRN: Si_7 N_3 above the two-photon absorption edge," Nat. Commun. 8(1), 1–10 (2017).

3. X. Sun, L. Zhang, Q. Zhang, and W. Zhang, "Si Photonics for Practical LiDAR Solutions," Appl. Sci. 9(20), 4225 (2019).

4. X. Sang, E. K. Tien, and O. Boyraz, "Applications of two photon absorption in silicon," J. Optoelectron. Adv. Mater. 11(1), 15 (2009).

5. C. L. Wu, Y. H. Lin, C. H. Cheng, S. P. Su, B. J. Huang, J. H. Chang, C. I. Wu, C. K. Lee, and G. R. Lin, "Enriching Si quantum dots in a Si-rich SiNx matrix for strong χ(3) optical nonlinearity," J. Mater. Chem. C 4(7), 1405–1413 (2016).

6. C. Torres-Torres, A. López-Suárez, L. Tamayo-Rivera, R. Rangel-Rojo, A. Crespo-Sosa, J. C. Alonso, and A. Oliver, "Thermo-optic effect and optical third order nonlinearity in nc-Si embedded in a silicon-nitride film," Opt. Express 16(22), 18390–18396 (2008).

7. R. Maram, S. Kaushal, J. Azaña, and L. R. Chen, "Recent trends and advances of silicon-based integrated microwave photonics," Photonics 6(1), 13 (2019).

8. A. Arbabi and L.L. Goddard, "Measurements of the refractive indices and thermo-optic coefficients of Si3 N4 and SiOx using microring resonances," Opt. Lett. 38(19), 3878–3881 (2013).

9. S. Grillanda and F. Morichetti, "Light-induced metal-like surface of silicon photonic waveguides," Nat. Commun. 6(1), 8182 (2015).

10. C. Lacava, S. Stankovic, A. Z. Khokhar, T. D. Bucio, F. Y. Gardes, G. T. Reed, D. J. Richardson, and P. Petropoulos, "Si-rich silicon nitride for nonlinear signal processing applications," Sci. Rep. 7(1), 22 (2017).

11. H. H. Lin, R. Sharma, A. Friedman, B. M. Cromey, F. Vallini, M. W. Puckett, K. Kieu, and Y. Fainman, "On the observation of dispersion in tunable second-order nonlinearities of silicon-rich nitride thin films," APL Photonics 4(3), 036101 (2019).

12. D. K. Ng, Q. Wang, T. Wang, S. K. Ng, Y. T. Toh, K. P. Lim, Y. Yang, and D. T. Tan, "Exploring high refractive index silicon-rich nitride films by low-temperature inductively coupled plasma chemical

vapor deposition and applications for integrated waveguides," ACS Appl. Mater. Interfaces 7(39), 21884–21889 (2015).

13. R. Sharma, M. W. Puckett, H. H. Lin, A. Isichenko, F. Vallini, and Y. Fainman, "Effect of dielectric claddings on the electro-optic behavior of silicon waveguides," Opt. Lett. 41(6), 1185–1188 (2016).

14. W. Bogaerts, P. De Heyn, T. Van Vaerenbergh, K. De Vos, S. Kumar Selvaraja, T. Claes, P. Dumon, P. Bienstman, D. Van Thourhout, and R. Baets, "Silicon microring resonators," Laser Photonics Rev. 6(1), 47–73 (2012).

15. G. F. R. Chen, J. W. Choi, E. Sahin, D. K. T. Ng, and D. T. Tan, "On-chip 1 by 8 coarse wavelength division multiplexer and multi-wavelength source on ultra-silicon-rich nitride," Opt. Express 27(16), 23549–23557 (2019).

16. H. Cong, Q. Feng, J. Zhang, J. Wang, W. Wei, T. Wang, and J. Zhang, "Kerr nonlinearity induced four-wave mixing of CMOS-compatible PECVD deposited ultra-Si-rich-nitride," J. Appl. Phys. 128(1), 013102 (2020).

17. S. Zhu, G. Q. Lo, and D. L. Kwong, "Low-loss amorphous silicon wire waveguide for integrated photonics: effect of fabrication process and the thermal stability," Opt. Express 18(24), 25283–25291 (2010).

18. M. J. Shaw, J. Guo, G. A. Vawter, S. Habermehl, and C. T. Sullivan, "Fabrication techniques for low-loss silicon nitride waveguides," Proc. SPIE 5720, 109–118 (2005).

19. P.R. Prasad, S.K. Selvaraja, and M. Varma, "Thermo-optic coefficient measurement of liquids using silicon photonic microring resonators," arXiv preprint arXiv:1710.03605, (2017).

20. C. J. Krückel, A. Fülöp, Z. Ye, and P. A. Andrekson, "Optical bandgap engineering in nonlinear silicon nitride waveguides," Opt. Express 25(13), 15370–15380 (2017).

21. X. Jiang, H. Wu, and D. Dai, "Low-loss and low-crosstalk multimode waveguide bend on silicon," Opt. Express 26(13), 17680–17689 (2018).

22. A. W. Elshaari, I. E. Zadeh, K. D. Jöns, and V. Zwiller, "Thermo-optic characterization of silicon nitride resonators for cryogenic photonic circuits," IEEE Photonics J. 8(3), 1–9 (2016).

23. J. Gong, R. Dai, Z. Wang, C. Zhang, X. Yuan, and Z. Zhang, "Temperature dependent optical constants for SiO2 film on Si substrate by ellipsometry," Mater. Res. Express 4(8), 085005 (2017).

24. J. T. Robinson, K. Preston, O. Painter, and M. Lipson, "First-principle derivation of gain in high-index-contrast waveguides," Opt. Express 16(21), 16659–16669 (2008).

25. J. T. Robinson, L. Chen, and M. Lipson, "On-chip gas detection in silicon optical microcavities," Opt. Express 16(6), 4296–4301 (2008).

26. J. Komma, C. Schwarz, G. Hofmann, D. Heinert, and R. Nawrodt, "Thermo-optic coefficient of silicon at 1550 nm and cryogenic temperatures," Appl. Phys. Lett. 101(4), 041905 (2012)

Chapter 3

Integrated Photonic Devices based SRN

3.1 Background

In the following, we look at the design, fabrication, and characterization of the integrated photonics components that could potentially be used in an integrated OPA design. Earlier in chapter 2 we demonstrated the high index, low loss, and high thermo-optic coefficient of our PECVD SRN films. Thus, we know that the design of low loss waveguides (i.e., splitters, couplers, and bends), power efficient and compact devices such as phase shifters and switches are possible.

The splitting and phase shifting architecture of one-dimensional OPAs can be divided into two categories. Generally, there is a cascaded phase shifter architecture and a tree-like architecture. There are of course advantages and disadvantages to using each architecture. We will discuss both and why we went with the simple tree like structure in our design.

In order to split and distribute the input light to a 1 x N network of antennas, cascaded 1 x 2 y branch couplers or 1 x N multimode interferometer can be implemented. Here we investigate the pros and cons and the performance of both designs.

Steering in an optical phased array happens by imposing a phase profile on the optical beam being transmitted/reflected. Controlling the phase and amplitude of each of the antenna arrays is very critical. The design of our SRN based optical phase shifters and MMI switch can be implemented to impose the appropriate phase/amplitude profiles. These modulations in optical phased arrays are typically done using the thermo-optic coefficient or the plasma-dispersion effect [1-3] in silicon waveguides. The phase shifters created by waveguide doping i.e., a PN junction, create a change in the refractive index which changes the phase of the light. However, since this is done by changing the carrier in the phase shifter, the optical loss

18

varies too. This causes the broadening of the spot size which is not ideal in phased arrays. In the case of our SRN films, due to the high thermo-optic coefficient, we show compact and efficient phase shifting where we have (8 mW per P_π) and 65 x 65 μm^2 of phase shifting area and similarly 23 mW per P_π and 68 x 68 μm^2. The small size of these devices makes them very useful for scaling and or cascading and provides a solution for the possible thermal crosstalk.

In order to achieve high beam efficiency and wide steering range of angles, we implemented end-fire facet waveguides at a half wavelength pitch specifically design to avoid coupling between the closely spaced waveguides. We do so by creating a phase mismatch between the neighboring waveguides. [4].

3.2 Splitter Design

3.2.1 Y-Branch Coupler

To distribute the light into different waveguide antenna arrays we have studied 1 x 2 y branch couplers. One of the reasons why cascaded y-branch couplers are often preferred to 1xN multimode couplers is due to equal power split in the output ports and that they are more compact in footprint. The MMI couplers can be more challenging to deal with in a phased array due to the inherent phase nonuniformity which will require phase compensation either actively or passively. This could potentially add more complexity to the system. However, we will investigate them in the next section as well.

We studied a simple adiabatic y branch coupler. In this case, the light is split equally into the two branches where the intensity is half of the input, and the electric field is $\frac{E}{\sqrt{2}}$- additionally, the phase difference between the branches is 90°. We used the inverse design method and the particle swarm algorithm to optimize the structure for the minimum insertion loss. The splitting section was designed such that it was very tolerant to fabrication imperfections.

Particle Swarm Optimization (PSO) is a technique which requires using a large set of iterations. In most cases of simulations, parameter sweeps work too, but particle swarm is very efficient since it is

designed to optimize for more than just one parameter and for a specific figure of merit [5]. PSO is best used as an algorithm for finding the minimum or maximum of a function defined on a multi-dimensional vector space. The brute force method of searching every possible combination for finding the solution to a minimum or maximum might be too expensive to do and practically impossible. However, if we could just randomly find some sample points on the plane for which the lowest/highest values of a function might exist. The operation of a PSO method also works on the basis of a random search. First, we start with a number of random variables (also referred to as "particles") and let them look for the minimum point in random directions. At every step, each particle should search around the minimum it found as well as the minimum found by the other particles. This is repeated for a certain number of iterations and thus, the minimum point found is then referred to as the minimum point found by this swarm of particles. It is important to note that the number of iterations can be either be fixed or dynamic in response to the progress i.e., we can make it stop if no changes are being made to the global best solution after a number of iterations. Here we use the insertion loss or $10 \times \log_{10}(2T_{avg})$ as the figure of merit/function we want to minimize for our y-couplers.

Our design is based on a polygon which is divided into 13 segments of equal length and different widths. The algorithm was used to optimize the number of sections into which the y-branch was divided. Here is the result of the optimized parameters for the segmented section:

Table 3.1. The splitter segmentation parameters (the width values here are in µm)

Splitter Length (µm)	W_1	W_2	W_3	W_4	W_5	W_6	W_7	W_8	W_9	W_{10}	W_{11}	W_{12}	W_{13}
3	0.4	0.4	0.4	0.4	0.4	0.6	0.88	0.87	1.6	1.6	1.26	1.25	1

As it can be seen from Table 3.1., the smoothened polygon shaped section has a 1.45 µm in width 3 µm in length and 200 nm separation between the splitting section. The geometry of this section is shown in Fig.3.1. (a). Fig.3.1(b) shows the SEM micrograph of the fabricated y-branch coupler. The 200 nm gap is very well defined, and the polygon is easily fabricated using E-beam lithography. The coupler was designed for TE-polarization with a simulated insertion loss of 0.159 dB. Using this relatively smoothened polygon as the splitter section makes the fabrication easy for scaling and integrating in tree-like structures in OPAs.

It is important that the optimization process is first carried out in 2.5D LUMERICAL MODE and further is tested to confirm the actual figure merit in a full 3D FDTD.
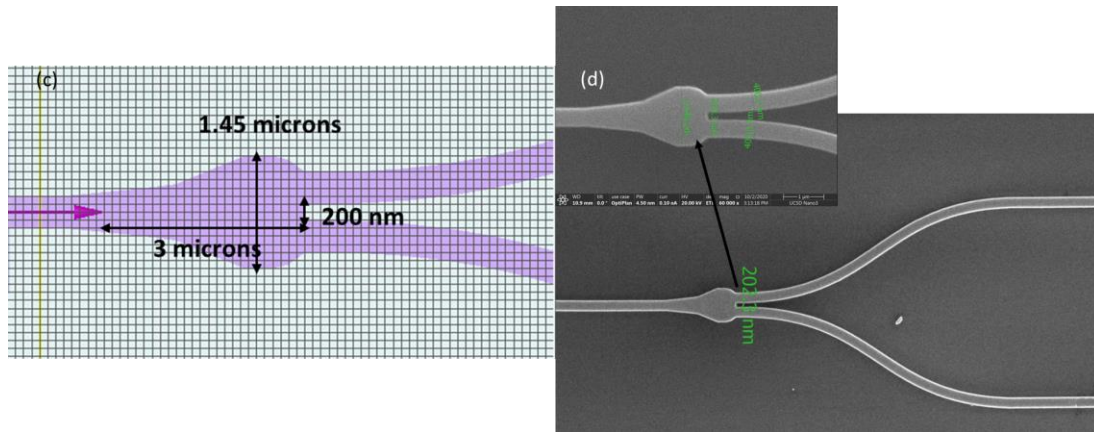
Figure 3.1. (a) The zoomed in schematic of the polygon designed for the splitting section of the Y-coupler (b) SEM micrograph of the Y-branch coupler
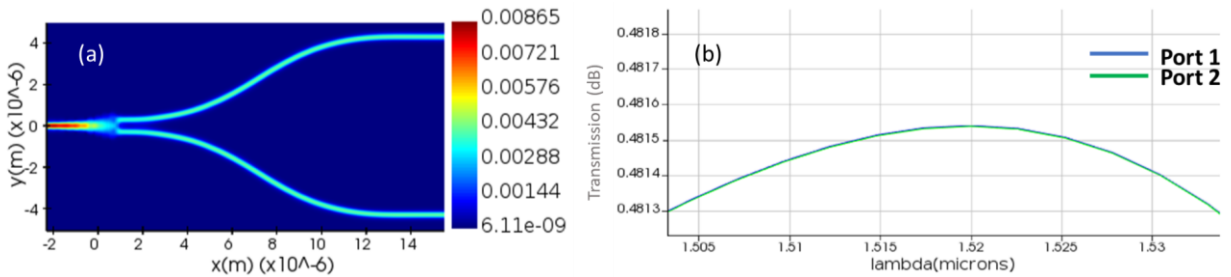
Figure 3.2. (a) Y-branch electric field intensity profile of the Y-branch coupler (b) The simulated transmission spectra of the plot shown in figure (a).

Using Lumerical full 3D FDTD simulation here we can see in Fig 3.2.(a) the intensity profile of the coupler showing an equal split of the optical power. Additionally, Fig. 3.2 (b) shows the simulated transmission spectra over a range of wavelengths from 1.5 to 1.54 μm. This shows broadband operation while maintaining relatively low loss.

The fabrication of the y-branch coupler here was carried out in a similar fashion to our previous work [6], using the PECVD deposited SRN film of n = 3.1, with the only difference being that in this case, the top cladding thickness is 1 µm.
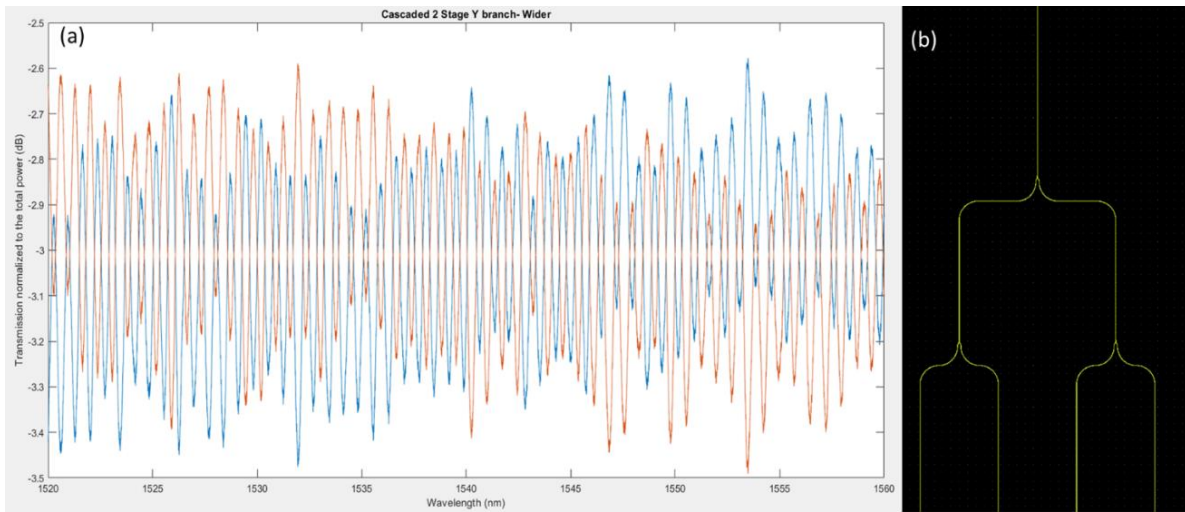
Figure 3.3. (a) The transmission spectra of the 2-stage cascaded y-branch couplers (b) The schematic of a 2-stage coupler

Further to investigate the splitter use in a phased array system, we implement a cascaded geometry. Here we show the schematic of a 1 x 4 splitter on the right in Fig 3.3.(a) and its transmission spectra in (b). We measured the top two ports of the device (due to the symmetry the bottom two ports are not shown) and the transmission plot shows a perfect split between the two. Note that the periodic swings here can be understood as the reflection from the end facets of the device which could lead to a cavity formation but since they are less than 0.5 dB from the -3 dB point (where the perfect split is), they can be tolerated. This process was repeated for 3,4, and 5 cascaded stages with similar performance.

Despite its perfect power split and compact footprint, cascading these y-branch couplers can lead to a large insertion loss. In our case for a 16-element phased array, cascading of 15 splitters means in our cases a total loss of 4.77 dB of loss. Instead, multi-mode interference splitters despite being less compact and requiring more sophisticated designs for better phase control, could be a great candidate for scaling and making efficient phased arrays. [7].

3.2.2 Multi-Mode Interferometric Coupler

Here, we design three different MMI splitters. A smaller 1x2, 1x4, and 1x8 for different stages of the OPA. Generally, MMIs consist of two parts, one is the center multimode waveguide and the access waveguides both at the input and the output. In all of our designs, there is a single waveguide at the input to a larger multi-mode waveguide following by two, four, and eight adiabatic linear tapers for the outputs respectively. The splitter's length and width are designed in such a way that when the higher order modes are excited the input electric field is self-image to the outputs. Tapered widths are not only useful for compactness, but also allows for increase in the light intensity near the dielectric corners with abrupt discontinuities and thus reduces the reflections. Additionally, an increase in the tapered width can improve the quality of self-imaging and thus reduces the excess loss. The imbalance and excess loss in MMI couplers are mainly determined by the way the input power is divided into the MMI's sectional modes, so the more adiabatic tapers provide a more acceptable transition and improves the quality of the self-image.

The imbalance between the outputs of the coupler and the insertion loss can be determined by the following equations:

$$imbalance = 10\log_{10}\left(\frac{P_1}{P_2}\right) \tag{1}$$

$$IL = 10\log_{10}\left(\frac{P_1+P_2+P_3+\cdots}{1}\right) \tag{2}$$

To obtain these results we use LUMERICAL MODE followed by FDTD to study our MMI coupler design, similar to the Y branch coupler. A desired design is achieved when there is minimum power

imbalance along with insertion loss. We use the three following parameters to design and optimize the structure. L_{MMI}, W_{MMI}, to define the length and width of the multimode waveguide, gap, L_{taper}, W_{taper}, to define the separation between the output waveguides and the taper length and taper width for controlling the gap between the output tapers and to determine the proper and equal split amongst the outputs. The optimized design ideally needs to have low insertion loss and low power imbalance between the output waveguides, so the figure of merit defined for the Particle Swarm algorithm is as follows:

$$Figure\ of\ merit\ (FOM) = \frac{\sum_{i=1}^{8} c_i}{(0.1 + \max(c_i) - \min(c_i))} \qquad (3)$$

Where c_i is the power transmission from the input waveguide to the output waveguide #i. Hence with that FOM, we use coupler length, coupler width, taper length, taper width, and the gap as parameters for the optimization. [8,9].

Table 3.2. The 1 x 2 MMI coupler parameters

Name	Value [μm]
Coupler Length	23.42
Coupler Width	5.16
Material	SRN
Separation	2.5
Taper Length	20
Taper Width	1.75
Total Length	80
Waveguide Width	0.4
Z span	0.305
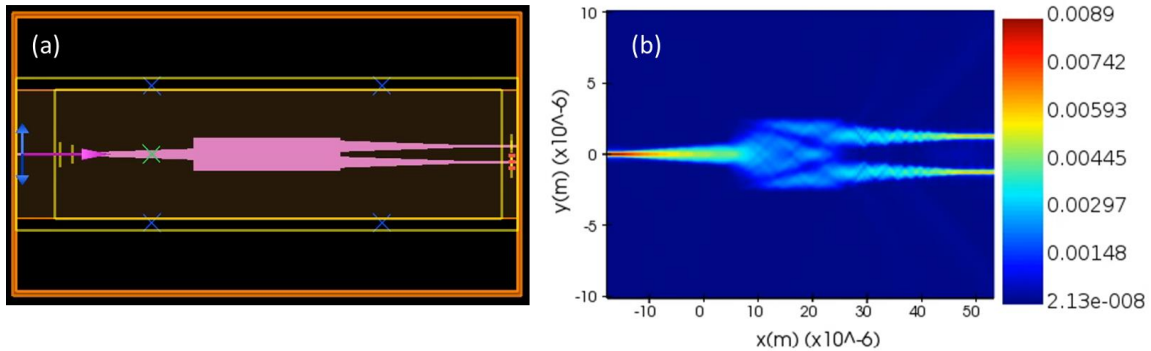
Figure 3.4. (a) The zoomed in schematic of the 1 x 2 MMI coupler (b) Electric field intensity profile of the coupler shown in (a)

In the case of the 1 x 2 MMI coupler, as shown in Table 3.2. the minimum coupler width is 5.16 μm, coupler length is 23.4 μm and the separation is 2.5 μm as shown in Fig. 3.4. The electric field intensity profile of the interference pattern of the 1x2 MMI is shown Fig. 3.4.(b). The transmission spectra of the simulated MMI coupler shows identical output for both ports with negligible imbalance. The insertion loss of 0.021 dB is calculated which in comparison with the traditional y-coupler design we showed in the previous section is 7.5 times more efficient in terms of optical loss.
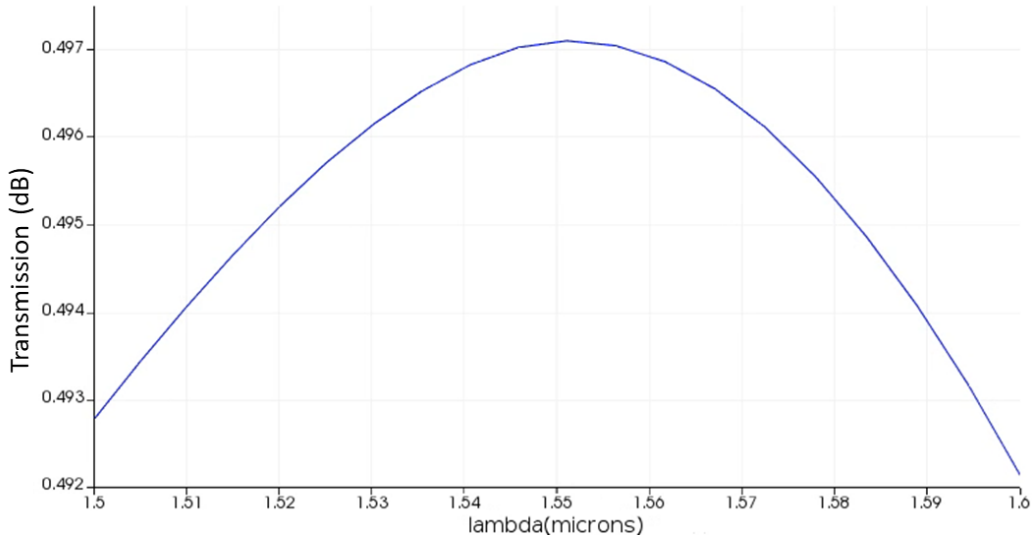
Figure. 3.5. The transmission spectra of the 1x2 MMI coupler

Table 3.3. The 1 x 8 MMI coupler parameters

Name	Value [μm]
Coupler Length	12
Coupler Width	8.8
Material	SRN
Separation	2.5
Taper Length	8
Taper Width	1.75
Total Length	54
Waveguide Width	0.4
Z span	0.305

In the case of the 1 x 8 MMI coupler, as shown in Table 3.3. the minimum coupler width is 8.8 μm, coupler length is 12 μm and the separation is 2.5 μm as shown in Fig. 3.6. The electric field intensity profile of the interference pattern of the 1 x 8 MMI is shown Fig. 3.6.(b). The transmission spectra of the simulated MMI coupler shows a power imbalance over the 0.1 µm wavelength range. The wavelength of operation is best to be chosen at 1.525 µm since the output powers are identical- this can be seen from the transmission spectra shown in Fig. 3.6. (c).
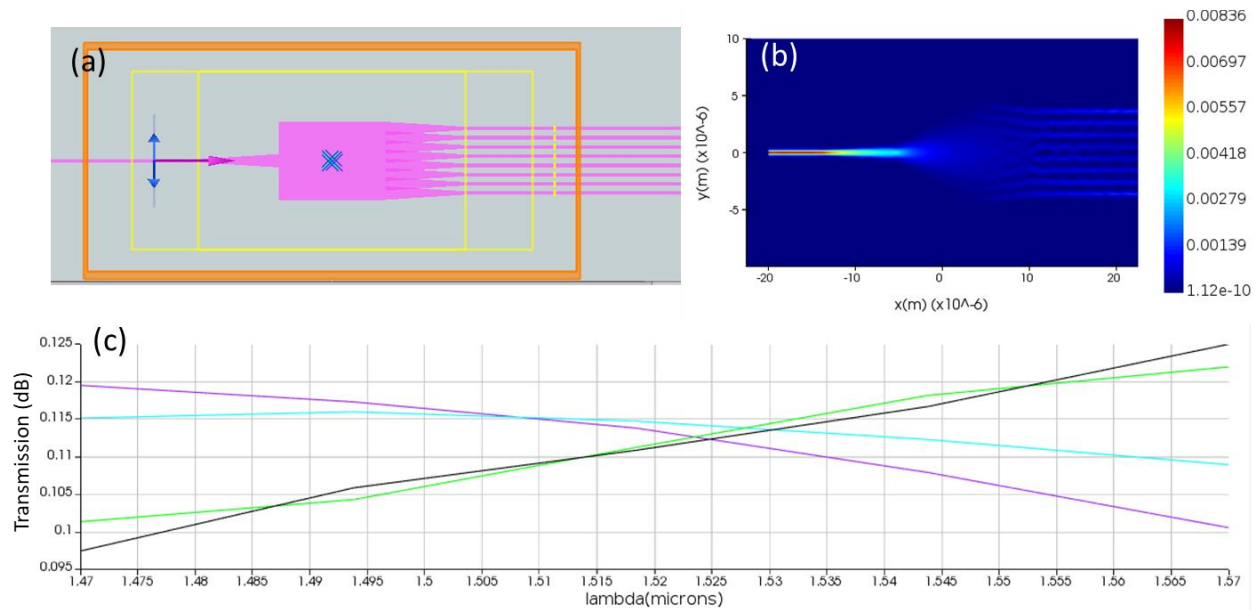
Figure 3.6. (a) The zoomed in schematic of the 1 x 8 MMI coupler (b) The electric field intensity profile of the coupler (c) the transmission spectra of the simulated

The insertion loss of 0.55 dB is calculated. In case of a cascaded Y-branch coupler with 8 outputs, the insertion loss is 1.33 dB which in comparison to our 1 x 8 MMI design is a factor of 2 more lossy. Although using an MMI coupler requires proper phase correction or operation at a wavelength where the optical outputs are equal, implementing them for an optical system where scaling is key i.e., OPAs helps with minimizing propagation loss in comparison to the more traditional designs such a y-branch coupler. [10].

The Optical Microscope (OM) image of the fabricated coupler is shown in Fig.3.7 (a). The fabrication process is similar to that shown in the previous sections for the coupler, ring, and MZI devices.

26

Fig. 3.7. (b) shows the IR camera image of the 8 outputs from the coupler during a wavelength sweep. Here the wavelength was at 1525 nm and shows consistency with the simulated results.
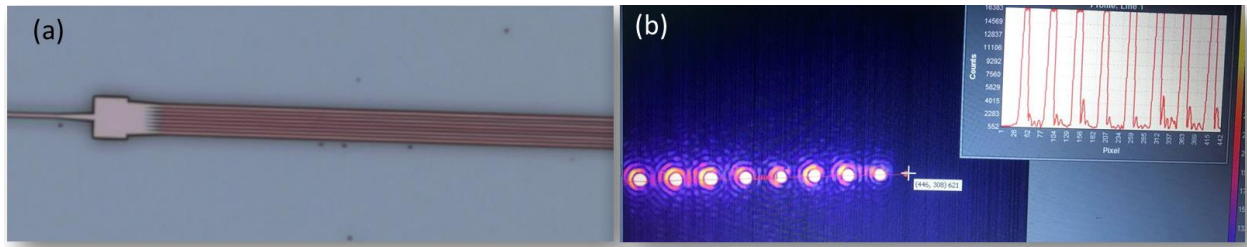
Figure 3.7. (a) The optical microscope image of the 1 x 8 MMI coupler (b) The optical modes of all 8 outputs measured and imaged with an Infrared camera

3.3 Multimode Interferometric Switch

To showcase the utility of the enhanced thermo-optic coefficient, high refractive index, and optical quality of SRN films such as S3, we demonstrate a novel thermo-optically tuned MMI switch in SRN designed for operation in the C-band. A schematic of the SRN MMI switch is shown in Fig. 3.8, where the active waveguide cross section is similar to that of the MZI in the previous section. The MMI switch operates by the interference of two modes in a 320 nm tall and 600 nm wide multimode SRN waveguide. The multimode waveguide was designed to support fundamental and first order TE-like modes while retaining low waveguide propagation loss for both. Using Lumerical MODE simulations, the effective index and confinement factor are 2.42 and 84% for the fundamental and 1.62 and 31% for the first-order mode respectively. The multimode section of the device has 300nm wide inlet and outlet single mode waveguides with 300 nm width as shown in Fig. 3.8. The smaller width of the inlet and outlet waveguides insure single mode operation. The input waveguides (straight and bent) were designed so as to equally excite the fundamental and first order modes directly in the active waveguide section. Two S-bends merge symmetrically and meet in the center of the MMI waveguide to adiabatically excite the first order mode in the MMI section in a manner similar to that done for other MMI switches using silicon [11,12]. The time averaged intensity profile in the MMI as well as the excitation sections are shown in the inset of Fig. 3.8.

The output portion of the switch, like the input section, consists of two single-mode, 45 µm bends which depart the MMI in an adiabatic fashion and form the two output ports. Depending on the effective optical length of the MMI for the two modes, the output of the MMI can be switched completely from one of the output ports to the other as shown in Fig. 3.8.
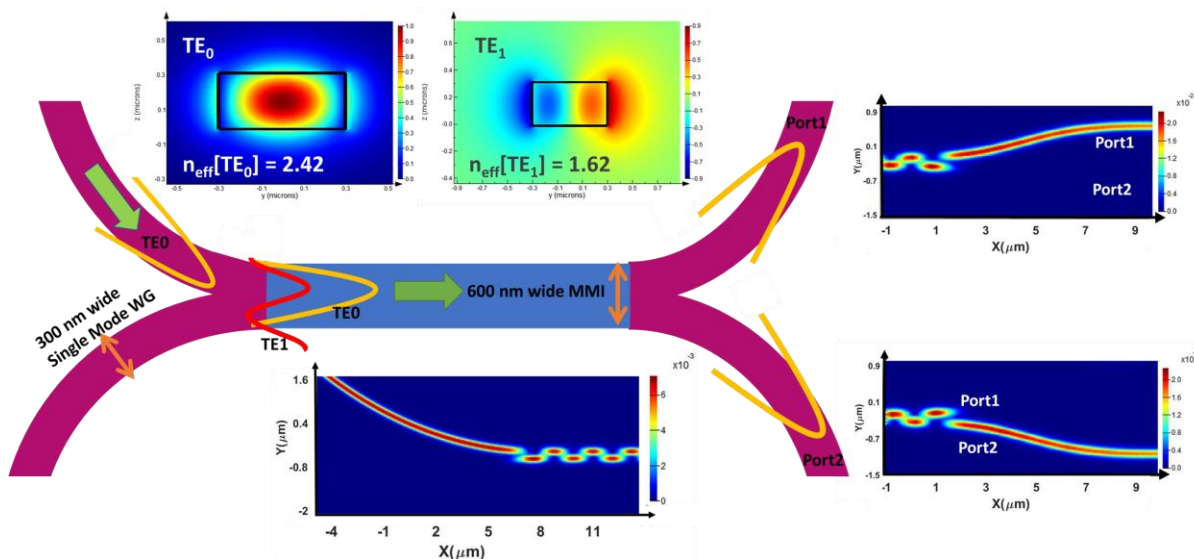
Figure 3.8. (a) Schematic representation of the MMI device showing the single mode symmetrical bends at the input with the propagating fundamental mode into the 600 nm wide MMI section with the propagating multi-modes and the single mode output bend waveguides. Inset shown are the fundamental and the first order TE modes propagating in the MMI with their corresponding effective indices and the 2D FDTD simulation of the MMI excitation from the tapered waveguide section of 300 nm in addition to the energy transfer between the output ports.

The characteristic beat length of the two MMI propagating modes is given by

$$L_B = \frac{\lambda}{2} \left[\frac{1}{n_{eff(TE_0)} - n_{eff(TE_1)}} \right] \tag{4}$$

where λ is the wavelength of the propagating optical field in vacuum, and $n_{eff}(TE0)$ and $n_{eff}(TE1)$ are the two modes' effective indices. A change in effective beat length of the two interfering modes can be actively induced by either changing the refractive index of the MMI waveguide material, or by changing the wavelength to achieve effective switching at the output ports. The former approach, in the case of SRN, can be induced by either utilizing its enhanced nonlinearity ($\chi^{(3)}$, using the well-known DC Kerr effect) [13] or exploit the enhanced thermo-optic effects as discussed below. The fabrication of the SRN MMI switch,

with an integrated Ni:Cr heater covering the multimode waveguide section, is carried out in a manner similar to that of the MZI in section 4. Optical switches with active SRN multimode waveguide sections as short as 800 µm was fabricated and characterized. The passive characteristics of the device, for an MMI section length of 800 µm, are shown in Fig. 3.9(a) as the measured normalized log-scale transmission at its two output ports as a function of wavelength. The characterization is carried out using the same setup as one used in section 4. As expected, the measured power at the two ports are conjugates of each other and show periodic peaks and valleys, with extinction ratios as high as 20 dB. The FSR of this response is measured to be approximately 3 nm. The FSR of such an MMI is expected to scale inversely with the length of the MMI and this is verified experimentally (not shown here) using fabricated devices of varying lengths.

It should also be noted, that achieving such high extinction ratios validates the use of symmetric bends at the input for the efficient excitation of the two interfering modes. Subsequently thermo-optic switching was observed by measuring the transmission at both ports as a function of power consumed by the heater element. The measurements were carried out at a fixed wavelength, $\lambda = 1517.95$ nm to maximize changes in output power as a function of index change. Fig. 3.9.(b) shows the individually normalized powers at the two ports as a function of power consumed in the heater element. As evident from Fig. 3.9.(b), upon application of power to the heater, the resulting change in temperature of the multi-mode waveguide, causes a change in output at both ports primarily as a result of thermo-optically induced change in refractive index of SRN. From these results one can observe that swings of up to 20 dB can be achieved in the output of individual ports and that the two outputs of the ports are exactly out of phase from each other, with the power required to completely switch the output from one port to another (defined as P_π) being ~50mW.
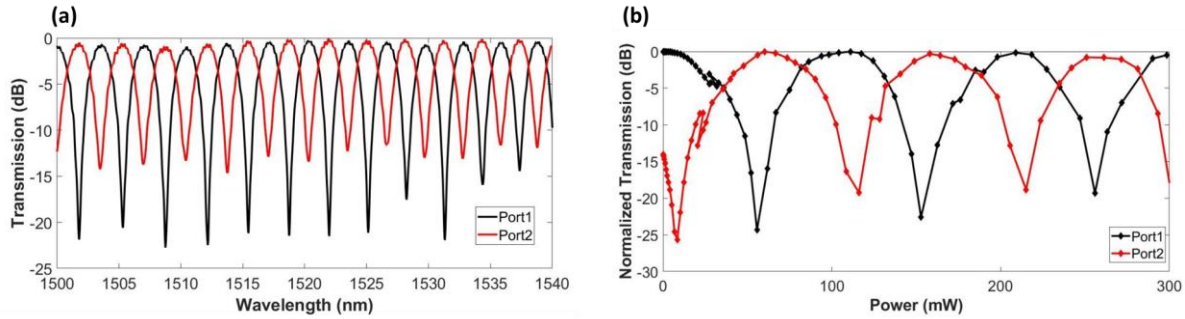
Figure 3.9. (a) Passive transmission spectra measured for 800 µm long MMI device for wavelengths of 1465 to 1570 nm (b) Transmission measured as a function of the power applied to the heater from 0 to 300 mW at λ = 1517.95 nm

Lumerical DEVICE was used to perform transient thermal simulations to estimate the expected time-dependent switching characteristics of the device [14]. As expected, the thick oxide cladding (∼2 µm) that separates the Ni:Cr heater from the waveguide and the 3 µm bottom oxide separating the waveguide from the silicon substrate, cause the device to have relatively high rise and fall times ∼50 µs. This implies a maximum switching rate of ∼10 kHz. It should be noted that this version of the SRN MMI switch was not optimized for switching speed. Dramatic reduction in rise and fall times can be obtained by switching to alternative heater configurations such as integrated doped silicon heaters, which allow for much lower separation between the waveguide and heating elements [14,15]. While the current version of this MMI has a straight multi-mode waveguide 800 µm in length, an optimized version can be designed with a combination of appropriately designed low-loss multimode straight and bend waveguides so as to allow for dramatic reduction in device footprint. In addition, the switching efficiency of this device can also be improved by a combination of detailed co-optimization of the active waveguide design and heater geometry and placement.

To further reduce the power consumption and footprint of thermo-optic switches, we exploited the design and optimization of multi-mode bends. We do so by utilizing these bends in a densely folded spiral waveguide structure of 1.2 mm total length with a total footprint of 68 x 68 µm^2 consisting of 5 and 7- µm bending radii for the 90 and 180-degree bends, respectively. Fig. 3.10. (a,c, and d) show the SEM

micrograph of the spiral MMI consisting of two 180º bends and twenty eight 90º implemented into the

MMI switching device shown in Fig. 3.10 (b) along with the Ni:Cr rectangular heater and the Cr/Au contact

pads.
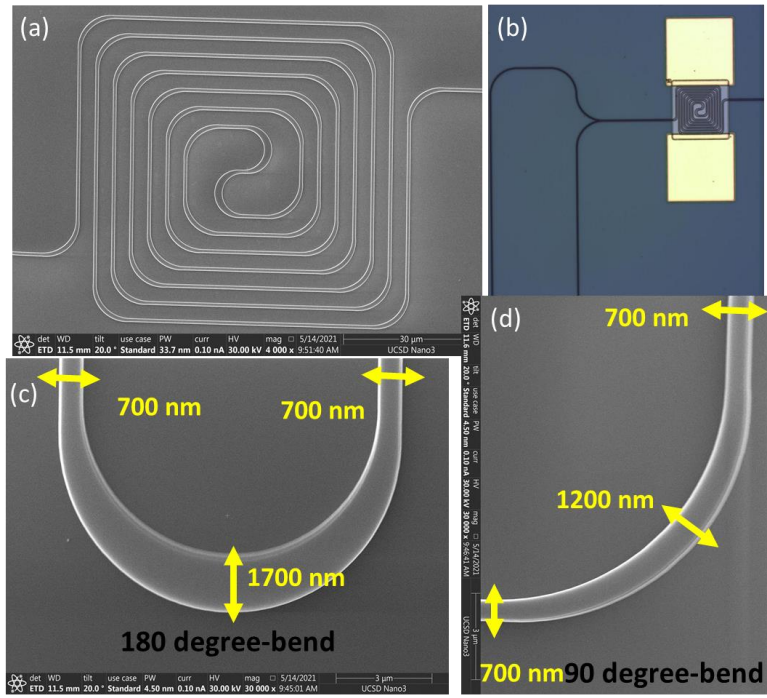
Figure 3.10. (a) SEM micrograph of the spiral consisting of 28 90º bends and 2 180º bends (b) the OM image of the MMI device with the implementation of the 1.5 mm spiral MMI c & d) SEM micrograph of the 180º and 90º bend with the input and output inlets of 700 nm with a transition to 1700 nm wide and 1200 nm wide mid-points respectively.

This structure allows for increased overlap of the waveguide with heater-induced temperature

distribution and hence a larger phase shift for a given applied thermal power.
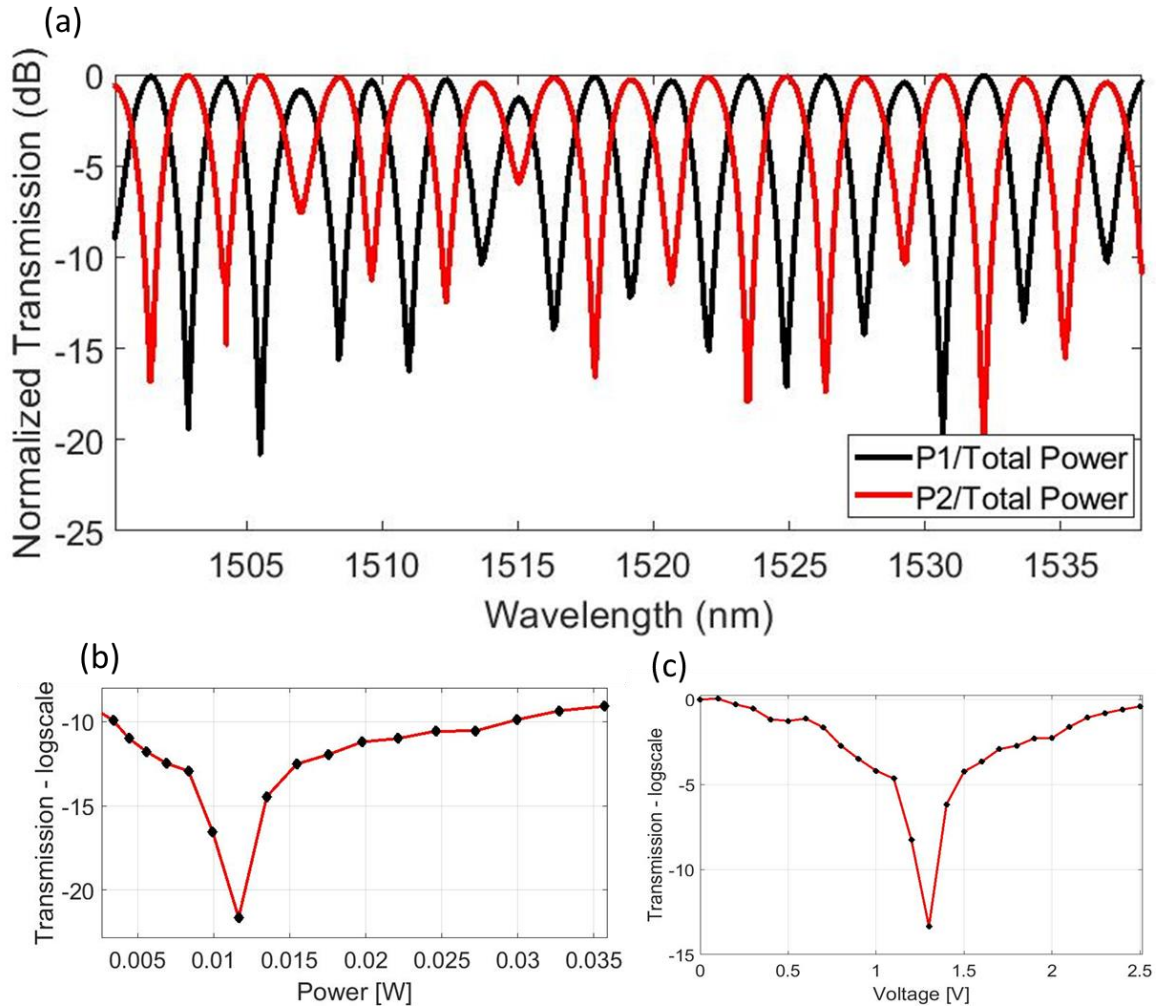
Figure 3.11. (a) Passive normalized transmission spectra measured for 1.2 mm long MMI device for wavelengths of 1500 to 1535 nm (b) The transmission as a function of the applied power to the heater- showing a $P_\pi = 23\ mW$ (c) the transmission as a function of the applied voltage with a $V_\pi = 1.25\ V$

The transmission spectra of this device were measured as shown in Fig. 3.11(a). As expected, the output of the two ports are conjugates of each other and change as a function of wavelength. The FSR of this device was measured to be around 2.8 nm. Note that achieving such high extinction ratios > 15 dB proves the equal excitation and low insertion loss for the two interfering modes. The heater power and the corresponding voltage required to switch from one port to the other was also experimentally measured. From Fig. 3.11.(b & c) the port to port switching power was experimentally shown to be $P_\pi = 23$ mW corresponding to a $V_\pi = 1$ V. From our previous work [6], a similar MMI with straight waveguide design

32

instead of that of the spiral structure with ultra-compact bends and small footprint, yields to a switching power reduction by a factor of more than 2 and footprint reduction by a factor of more than 5.

It is important to note that, since the bent waveguides have a different group index than the straight section. The FSR and the P_π won't scale linearly.

$$FSR = \frac{\lambda^2}{\Delta n_{g_{total}} L} \tag{5}$$

Where the group index is a combination of the group index of both straight and bend waveguide sections

$$\Delta n_{g_{total}} = \left(\Delta n_{g_{straight}} \times L_{straight}\right) + \left(\Delta n_{g_{bend}} \times L_{bend}\right) \tag{6}$$

Similarly, to the spiral structure, in the case of a serpentine shown in Fig. 3.12 (a) with the same length of 1.2 mm, the FSR of 3.3 nm and a P_π of 26 mW is observed. The passive transmission spectra of the device Fig. 3.12 (b) with extinction ratios > 15 dB is shown proving the low insertion loss and broadband operation of the device and scalability of these multimode bent waveguides.
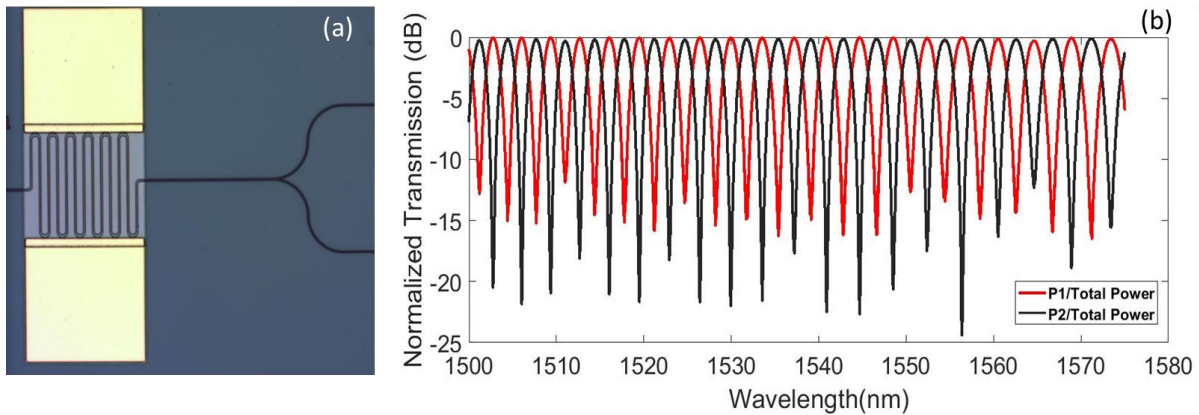
Figure. 3.12. (a) The OM image of the MMI device with the serpentine of ~ 1.2 mm- an alternative design to the spiral based MMI (b) The passive transmission spectra of the serpentine based MMI with each port normalized to the sum of the powers in the two ports

33

Table 3.4. The theoretical and experimental ratios of the FSR for all the three different MMI
configurations: straight, spiral, serpentine

FSR Ratios	Analytical	Experimental
Spiral to straight	0.96	0.96
Spiral to serpentine	0.92	0.9
Serpentine to straight	1.05	1.1

In the table shown (Table 3.4.), the theoretical ratio of the FSR in the cases of the straight, spiral, and serpentine structures are compared to that of the experimental one. The results confirm that the major source of this difference in the FSR is indeed due to the variations in the number of straight and bent waveguide sections.

3.4 Compact bend structure

In the previous section we showed that to further reduce the power consumption and footprint of thermo-optic switches, we could exploit the design and optimization of multi-mode bends. In this study, we use one of our highly silicon-rich SRN films with n = 3.1 (at λ = 1550 nm) to enable the design of ultra-compact bends. The ultra-compact bends are then used to wrap waveguides in a rectangular spiral fashion for maximizing the length of the waveguide under the metallic heater. The design of 90 and 180-degree bends was hence critical. The bends designed are modified Euler Bends [17-20] and optimized using particle swarm algorithm [21]. Both the 90- and the 180-degree bends are defined by parameters r_{min}, r_{max}, which are the distances of the inner and outer edge of the waveguide with respect to the bend center and are related by the following relation:

$$r_{max} = r_{min} + f(\theta) \tag{7}$$

$$f(\theta) = w_{max} + (w_{min} - w_{max}) \times \frac{ln(cosh(c \times \theta_0) - c \times \theta)}{ln(cosh(c \times \theta_0))} \tag{8}$$

Where θ_0 is a constant, $\pi/4$ for the 90 degree and $\pi/2$ for the 180-degree bend, θ is the angular position along the bend, w_{min} is the width at the start and end of each bend, w_{max} is the width of the bend at the halfway mark i.e., 45 degrees and 90 degrees for 90 and 180-degree bends respectively. Note the width of the bend at the start and the end is the same and the inlet and outlet waveguides are also kept at the same width, w_{min}. The asymmetry constant, c, is determined optimally according to the averaged radius of curvature.

To maintain low loss performance, the width of the waveguide is constantly varied in the bend. This is described by $f(\theta)$. The function $f(\theta)$ is chosen such that the increase in width is very gradual so as to avoid any excess loss as described in Eq. (3). For a given w_{min} optimization of insertion loss was carried out by using particle swarm algorithm and 2.5 D FDTD simulations in LUMERICAL MODE to determine parameters, maximum waveguide widths (w_{max}), the constant c, and bend radii, r_{min}. The same study is done for the 180-degree bend. We do so for both single and multi-moded bent waveguides.
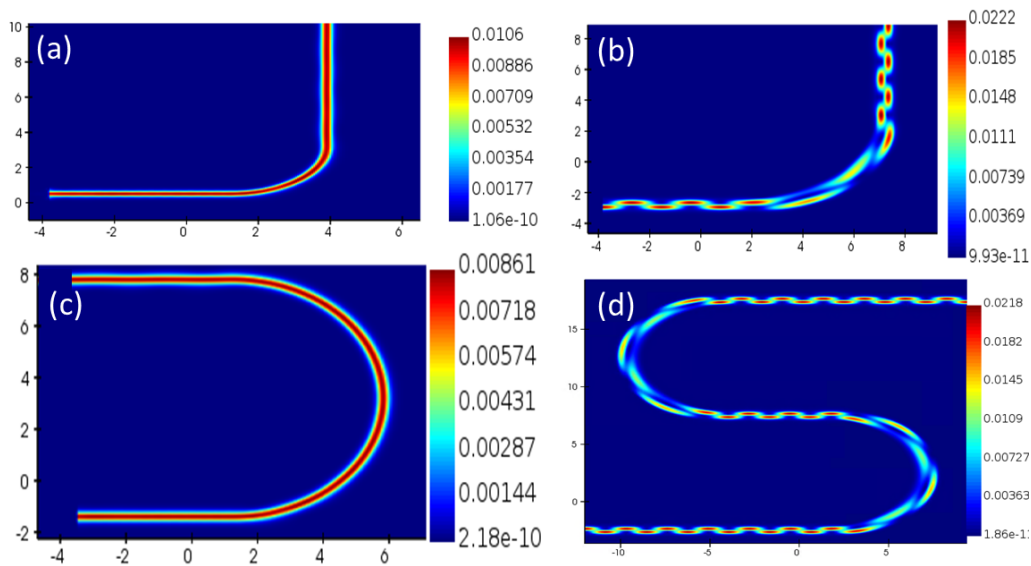
Figure. 3.13. (a) Passive transmission spectra measured for 800 μm long MMI device for wavelengths of 1465 to 1570 nm (b) Transmission measured as a function of the power applied to the heater from 0 to 300 mW at λ = 1517.95 nm

In the single mode case, the optimized 90-degree bend with an effective bend radius $r_{effective} = 4.1$ μm and $w_{max} = 0.41$ was then confirmed to show a low insertion loss of 0.025 dB using full 3D FDTD

simulation as shown in Fig.1(a). Fig.1(b), shows the simulation results for a similarly optimized 180-degree bend with an $r_{effective} = 4.4$ µm and $w_{max} = 0.42$ µm, showing an insertion loss value of 0.026 dB. In the multi-mode case, the optimized 90-degree bend with an effective bend radius $r_{effective} = 7$ µm and $w_{max} = 1.2$ mm was then confirmed to show a low insertion loss of 0.07 dB using full 3D FDTD simulation as shown in Fig.1(a). Fig.1(b), shows the simulation results for a similarly optimized 180-degree bend with an $r_{effective} = 5$ µm and $w_{max} = 1.7$ mm, showing an insertion loss value of 0.06 dB.

3.5 SRN based thermo-optic phase shifter

Phase shifters are important components for many optical signal processing applications, including optical phased arrays (OPA) for beam steering and light detection and ranging (LiDAR) [22]. Such optical systems have a vast set of design requirements [23,24]. Design challenges of photonic integrated circuits (PICs) include maintaining low insertion loss, low power, small footprint, and fast response time while integrating substantial number of components. To meet these performance requirements, it becomes essential to optimally select an appropriate material platform.

For example, high optical power is required in an OPA chip to maximize receiver signal-to-noise ratio. This means a material platform with low two photon absorption (TPA) is ideal. Additionally, to maintain compactness, scalability, high efficiency, and low loss phase shifting, a high index contrast platform with high thermo-optic coefficient is needed.

Silicon-on insulator (SOI) is predominantly used as a CMOS compatible material platform for silicon photonics devices and applications. Due to the high index contrast between silicon and silicon dioxide, SOI enables fabrication of passive components such as compact bends, splitters, and interferometers. Moreover, silicon possesses a high thermo-optic coefficient of (1.86×10^{-4} K^{-1}) that makes it a viable candidate for thermo-optical phase shifters. However, silicon has its own drawbacks such as a relatively narrower transparency window (1.1 to 8 µm), TPA, and surface carrier absorption (SCA) leading

to low power handling capabilities [23,25,26]. To overcome some of the limitations of silicon, stoichiometric silicon nitride (Si3N4) is often used as another CMOS compatible platform [27,28]. It has a larger transparency window (0.25 to 8 µm) and possesses negligible TPA unlike silicon. However, it has a lower thermo-optic coefficient ($\sim 2 \times 10^{-5}$ K^{-1}) and a lower refractive index (~ 1.98), leading to inefficient optical phase shifters and larger footprint, respectively [23,29]. In light of this, SRN platform is an increasingly attractive CMOS compatible alternative for applications where the benefits of both silicon and stoichiometric silicon nitride are desired. [30,31]. Due to the high degree of tunability of its refractive index and thermo-optic coefficient (n = 3.1 and dn/dT =1.65x10^{-4} K^{-1} at λ = 1550 nm [32]), SRN can be a viable candidate for highly efficient, small footprint devices that require high optical power handling capabilities.

In this investigation, we present means to reduce the power consumption and the footprint of thermo-optic phase shifters by exploiting the design and optimization of ultra-compact bends in SRN. These bends are the structured in a densely folded rectangular spiral of 1.2 mm total length with a total footprint of 65 x 65 µm^2. For the phase shifter characterization, we use the spiral structure as one of the arms of an unbalanced Mach Zehnder Interferometer (MZI) with serpentine shaped heaters. The experimentally demonstrated device exhibits a P_π = 8 mW, a V_π = 1.5 V, with extinction ratio exceeding 15 dB proving to be a promising device for thermo-optic applications requiring efficiency, compactness and high-power handling capabilities.

The thermally induced phase shift for a phase shifter can be represented by:

$$\Delta\phi = \frac{2\pi}{\lambda}\left(\frac{\partial n_{eff}}{\partial T}\right)\Delta T \, L_{mod} \qquad (9)$$

where λ is the wavelength of the guided optical mode (in this case 1550 nm), $(\partial n_{eff})/(\partial T)$ is the change in the effective index as a function of temperature change, L_{mod} is the active length of the device and ΔT is the temperature change across the active length. As seen from the Eq. (1), to achieve efficient phase shifting, a material platform which can provide a large $(\partial n_{eff})/\partial T$ is desirable. SRN has this property as its thermo-

optic coefficient is close to that of crystalline silicon (1.65 ± 0.08) x 10^{-4} K^{-1} [32]. In a typical straight waveguide-based phase shifter, increasing the active length of the device will linearly increase the phase change, however at the cost of increased power consumption and slower switching speeds. It would hence be highly desirable to develop ultra-compact bends so as to increase waveguide packing density and achieve a high active length while keeping the heater footprint to a minimum. [33-36].

To exploit the small bend radii achieved using the high index SRN and demonstrate efficient thermo-optic phase shifting, we utilized the bends to realize the rectangular spiral. The spiral of 1.2 mm total propagation length consists of twenty-seven 90-degree bends and two 180-degree bends packed into an area of 65 x 65 µm2. The Y-branch designed and fabricated for TE-polarization with a simulated insertion loss of 0.159 dB shown earlier in this section was used to fabricate the MZI structure input and output coupling sections. From our previous measurements in [6], the propagation loss for TE polarized optical mode in our SRN waveguides is ~7 dB/cm). While we did not carry out an experimental measurement for the loss in our bends in the complete spiral, the simulated value of loss in our bends can be used to estimate a lower bound for the total insertion loss associated for one such spiral structure to be around~ 1.2 dB.

The fabrication of the thermo-optic phase shifters is carried out in a similar fashion to our previous work [6], using the PECVD deposited SRN film of n = 3.1, with the only difference being that in this case, the top cladding thickness is 1 µm.

To study the effect of the metallic heater geometry on the performance of the phase shifter, a serpentine and a rectangular configuration are evaluated. Fig. 3.14(a) and (b) show the optical microscope (OM) top view of the two configurations integrated onto the spiral phase shifting section of an MZI. The serpentine heater consists of six filaments of 6 µm in width separated by 8 µm; this allows for higher resistance in a compact area, whereas the latter heater is simply a rectangle of 100 x 80 µm2. Both configurations have

the same metallic (Ni:Cr) thickness of 300 nm. The serpentine heaters were designed in such a way so as to achieve a long metallic filament over the rectangular spiral. The width of the metallic filament and the separation between them were chosen so as to ensure a high value of resistance and fairly uniform temperature profile across all the waveguides while ensuring the ease of fabrication.

Fig. 3.14(c) shows the distribution of temperature along a cutline passing through the center of waveguides under the metallic heater for the serpentine configuration. Fig. 3.14(d) shows the corresponding 2D profile of the temperature distribution in a cross section for a heater power of 8 mW. The thermo-optic simulations were carried out using LUMERICAL DEVICE. As expected, waveguides positioned in between the metallic lines (as opposed to directly underneath) experience a slightly lower temperature (97%) than the ones positioned directly underneath the metallic lines [31,33-36].

This ensures temperature uniformity across the spiral waveguide. Similar simulation studies (not shown here) are carried out for the rectangular heater shown in Fig 3.14(b).
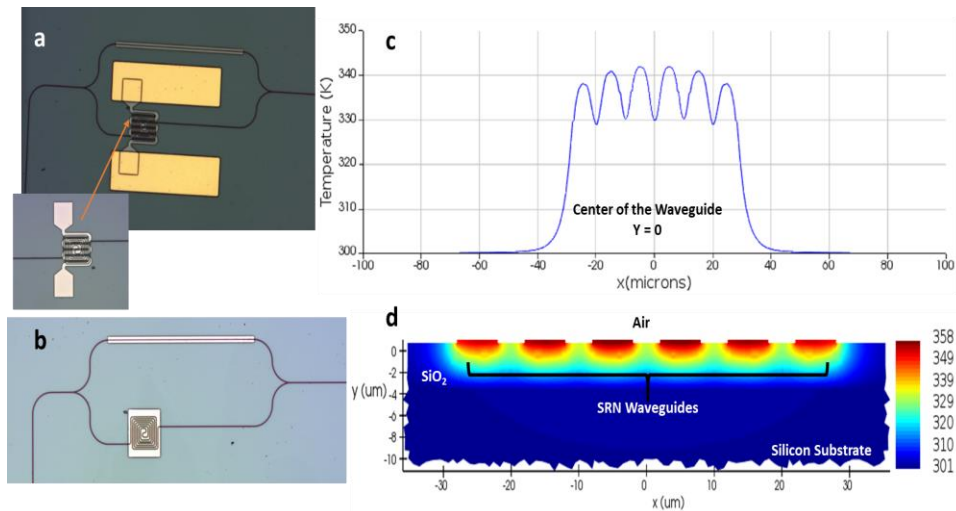
Figure 3.14. (a) OM top view of the MZI with the spiral as its imbalanced length along with the integrated Ni:Cr serpentine heaters and Cr/Au contact pads -the zoomed-in OM image of the spiral waveguide with the Ni:Cr serpentine heater on top(b) OM top view of the MZI with spiral waveguide and a rectangular Ni:Cr heater on top(c) temperature distribution along a cutline in the plane of the waveguides at y = 0 (d) Simulated temperature profile in a cross-section of the spiral waveguide

To characterize the phase shift as a function of heater power dissipation, the thermo-optic phase shifter is fabricated as part of one arm of an unbalanced MZI. The devices shown in Fig. 3.14(a, b) are characterized

using a fiber-in free space out setup such as that employed in [6]. The estimation of P_π was done by operating the device at a fixed wavelength and measuring the output transmission as a function of the power applied to the heater as shown in Fig. 3.15(a) for a device with a serpentine heater. The power range of 0 to 35 mW corresponds to a voltage applied of up to 4 V, and the extracted Pπ is 8 ± 0.25 mW ($V_\pi = 1.5 \pm 0.25$ V) with an extinction ratio exceeding 15 dB. The corresponding values for a device with a rectangular heater are $P_\pi \sim 11.5 \pm 0.25$ mW. Fig. 3.15 (b) shows the spectral shift in the transmission of the MZI as a function of the applied voltage (0 to 1.8 V). The transmission spectra were measured in a range of 1465 nm to 1575 nm (using a CW tunable Agilent laser in the C-Band) showing an FSR of ~ 0.56 nm. The frequency response of the device is characterized by applying a square wave signal (1.5 V amplitude) to the heater such that a π phase shift could be achieved. To do so, we use a 15 MHz Hewlett-Packard waveform generator. The frequency of the square wave signal was swept from 0.5 to 25 kHz and the peak-to-peak voltage response was recorded at each step. The 3-dB bandwidth of the phase shifter was measured to be 15±0.5 kHz as shown in Fig.3.15(c). While the 3-dB is currently low however it should be noted that no optimization has currently been carried out with regards to optimizing the speed of the device. Similar measurements are carried out for the rectangular heater, and no significant changes to the 3-dB cutoff frequency is observed. The uncertainties in the measured values for the Pπ, Vπ and the 3-dB bandwidth arise from the statistically measured standard deviation of over 15 repeated measurements.

The experimental characteristics of the demonstrated device are promising and can be further improved by optimization of the heater electrode and cladding design. The reduced power consumption of the spiral structure with the serpentine heaters is due to the laterally diffused heat from the heater filaments and the increased fraction of waveguide length per heated area.
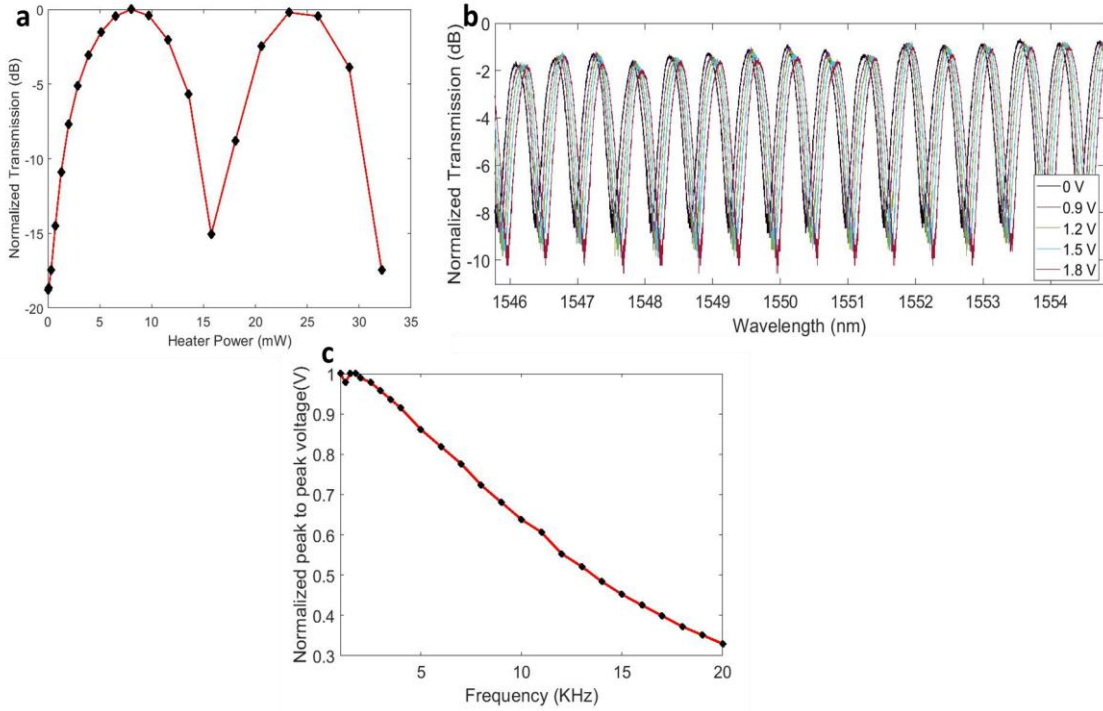
Figure 3.15. (a) Experimental result on the transmission of the MZI as a function of the switching heater power demonstrating a $P_\pi = 8$ mW. The measurements were carried out at a fixed wavelength, $\lambda = 1551.5$ nm to maximize changes in output power as a function of index change (b) Spectral shift of the null point in transmission due to the applied voltage from 0 to 1.8 volts (c) 3-dB cutoff frequency of the device measured to be ~ 15 kHz

Table 3.5. Comparison summary of thermo-optic phase shifters

Material	β_{TPA}(cm/GW) ($\lambda = 1550$ nm)	Optical Power Handling	P_π(mW)	Area (mm^2)	Ref.
Silicon (Doped Waveguide)	0.5 [2]	Low	24.77	0.0015	18
			3	0.0018	16
SRN (Ni:Cr Heater)	Negligible [20]	High	8	0.0016	This work
Stoichiometric silicon nitride (TiN Heater)	Negligible [21]	High	65	0.7	8
			87.65	0.001	22

The observed performance of the device proves that SRN's high refractive index and high thermo-optic coefficient allow for both compact and efficient phase shifting. Furthermore, SRN phase shifter can be a more desirable option compared to silicon, for applications requiring high optical power handling capabilities and scalability (e.g., OPAs). This is because, as listed in Table 3.5, SRN (even with a high

silicon content and index of up to 3.1) exhibits negligible TPA much lower than that of silicon. Thus, SRN is a great choice for realizing efficient, low footprint, and high optical power handling devices.

In this work we present the design, fabrication, and characterization of ultra-compact single mode bends using silicon rich nitride. We then use these bends to demonstrate a highly efficient, low footprint SRN thermo-optic phase shifter consisting of a rectangular spiral with integrated serpentine Ni:Cr heaters. The densely folded spiral structure has a 1.2 mm total length with a total footprint of 65 x 65 µm2 consisting of ultra-compact 90 and 180-degree bends with effective radii of 4.1 and 4.4 µm respectively. The folded structure allows for an increased overlap of the waveguide with temperature distribution from the integrated serpentine heater and hence a larger optical phase shift to be induced for a given applied thermal power. Two heater geometries were investigated, one a simple rectangle over the spiral waveguide region and the other a serpentine heater. The latter is shown experimentally to outperform the rectangular heater by 30% in terms of its Pπ. The serpentine heater over the phase shifter exhibits a $P_\pi = 8$ mW and a $V_\pi = 1.5$ V with an extinction ratio ~ 15 dB. This new thermo-optic phase shifter design enables precise targeting of power dissipation and heat localization, resulting in low thermal crosstalk and high efficiency. The combination of the high index and high thermo-optic coefficient enables not only a compact and efficient phase shifter, but also proves to be the most promising device for applications requiring scalability and high optical power handling capabilities

3.6 Closely spaced waveguide

In order to achieve high beam efficiency and wide range of steering, the end fire facet waveguides are designed to achieve $\frac{\lambda}{2}$ spacing. However, to avoid coupling between the waveguide antennas for long propagation lengths (over mm scale), we can minimize their overlap in the phase space by creating a mismatch in their β coefficients. We did so by designing and fabricating waveguides of different widths. Their widths were chosen carefully and was kept in a similar range of values to ensure uniform illumination

across the array. In this thesis, two configurations were studied. In the first case which is also later used in the final design of our OPA chip, the waveguides are phase mismatched with both their nearest neighbor and with their second nearest neighbor (separated by $\frac{\lambda}{2}$ and λ, respectively) by cycling through a set of three widths (300, 400, 500 nm in sequence). Third nearest neighbors are separated by $\frac{3\lambda}{2}$ and have equal widths. This is possible since the power coupling between two neighboring waveguides changes as a function of $\frac{1}{\left(\frac{\Delta\beta}{2\kappa}\right)^2+1}$ where $\Delta\beta$ is the difference in propagation constant and κ is the coupling coefficient (field overlap coupling strength), thus this modeled phase mismatch between the closely spaced waveguides ($\Delta\beta$) allows for weak coupling between them even if their evanescent tails are overlapping. Also, keeping the height of all of these waveguides the same and at 320 nm, ensures single-mode for TE-polarized light across the entire propagation length. [37].

Lumerical EME simulation of the waveguide array with sequentially varying widths of 500, 300, 400, and 500 nm is shown Fig. 3.16 (a-b). Light is launched into the 500 nm wide waveguide, the eigenmode expansion shows less than 2% coupling only to the waveguide with equal width. Further, the S-parameters for the transmission from waveguide one, 500nm to waveguide five, its equal width

waveguide, are shown in Fig. 3.16 (c-d) for a 1mm length propagation direction showing minimal coupling.
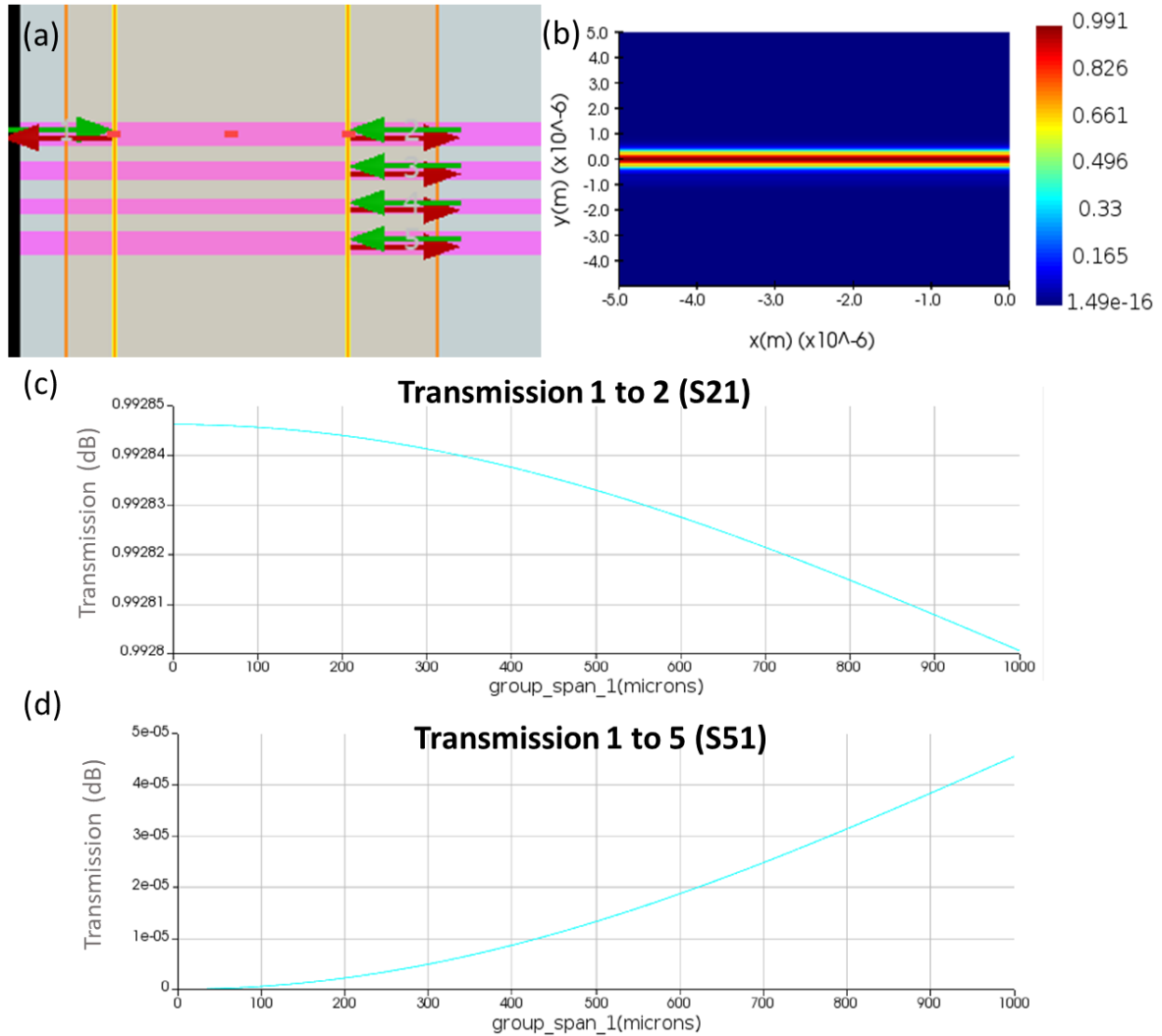
Figure 3.16. (a) The closely spaced waveguide schematic of the EME simulation showing the source launching at waveguide 1 and the alternating waveguide widths are spaced at $\frac{\lambda}{2}$ spacing (b) the transmission of light from port 1 to port 2 showing no coupling to the neighboring waveguides. This is obtained for 1 mm propagation length (c & d) show the S-parameter from port 1 to 2 where the maximum transmission happens and port 1 to 5 where there is basically no transmission happening

Here in Fig. 3.17. we experimentally demonstrate that even for several-mm propagation lengths, coupling between nearest, second nearest, and third-nearest neighbors is below 18-22 dB and power propagates only in the waveguide into which light was launched.

44
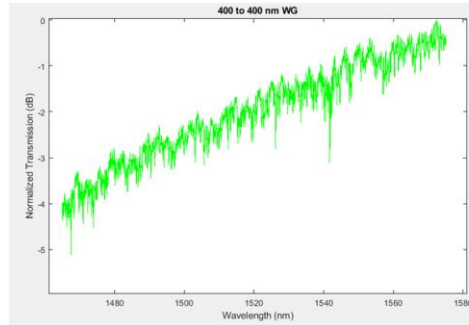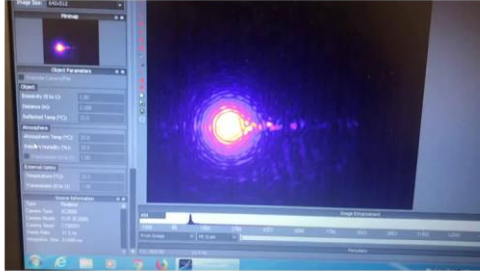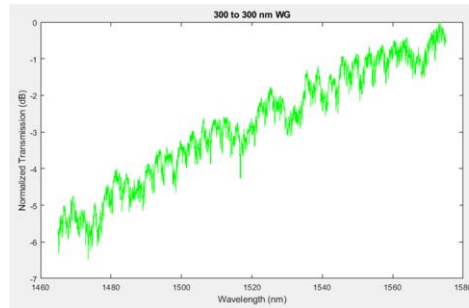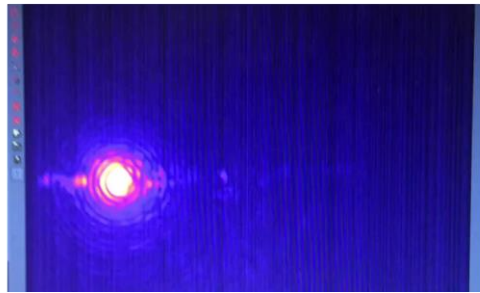
Figure 3.17. The IR image of the mode profile of the closely spaced waveguides and their corresponding transmission plots as a function of wavelength. Showing minimal coupling to the neighboring waveguide < 18-22 dB

3.7 Conclusion

In conclusion, we have shown design, simulation, fabrication, and characterization of the integrated photonic components that were possible to make given our PECVD SRN platform. The above results were an essential part of the design for an optical phased array chip. The optimization and characterization of each device is significant because that will translate into what the design limitations and capabilities of our OPA chip are. Additionally, the work shown here demonstrates a few state-of-the-art devices that could potentially be used as standalone components for thermo-optic and integrated photonics applications.

Chapter 3, in part, contains materials from ""Efficient and compact thermo-optic phase shifter in silicon-rich silicon nitride", published in Optics Letters and co-authored by S. Pappert, Y. Fainman, and P. Yu. The dissertation author was the first author of the manuscript.

Bibliography

Chapter 3

1. M. Jacques, A. Samani, E. El-Fiky, D. Patel, Z. Xing, and D. V. Plant, "Optimization of thermo-optic phase-shifter design and mitigation of thermal crosstalk on the SOI platform," Opt. Express 27, 10456-10471 (2019)

2. G. Coppola, L. Sirleto, I. Rendina, and M. Iodice, "Advance in thermo-optical switches: principles, materials, design, and device structure," Opt. Eng. 50(7), 071112 (2011).

3. D. Thomson, A. Zilkie, J. E. Bowers, T. Komljenovic, G. T. Reed, L. Vivien, D. Marris-Morini, E. Cassan, L. Virot, J. M. Fédéli, J. M. Hartmann, J. H. Schmid, D.-X. Xu, F. Boeuf, P. O'Brien, G. Z. Mashanovich, and M. Nedeljkovic, "Roadmap on silicon photonics," J. Opt. 18(7), 073003 (2016).

4. C.T. Phare, M.C. Shin, S.A. Miller, B. Stern, and M. Lipson, 2018. Silicon optical phased array with high-efficiency beam formation over 180-degree field of view. arXiv preprint arXiv:1802.04624.

5. D. Wang, D. Tan, and L. Liu, 2018. Particle swarm optimization algorithm: an overview. Soft Computing, 22(2), pp.387-408.

6. H. Nejadriahi, A. Friedman, R. Sharma, S. Pappert, Y. Fainman, and P. Yu, "Thermo-optic properties of silicon-rich silicon nitride for on-chip applications," Opt. Express 28, 24951-24960 (2020).

7. A. Maese-Novo, R. Halir, S. Romero-García, D. Pérez-Galacho, L. Zavargo-Peche, A. Ortega-Moñux, I. Molina-Fernández, J.G. Wangüemert-Pérez, and P. Cheben, 2013. Wavelength independent multimode interference coupler. Optics express, 21(6), pp.7033-7040.

8. L.B. Soldano, L.B. and E. C. Pennings, E.C., 1995. Optical multi-mode interference devices based on self-imaging: principles and applications. Journal of lightwave technology, 13(4), pp.615-627.

9. M. Bachmann, P.A. Besse, and H. Melchior, 1994. General self-imaging properties in N× N multimode interference couplers including phase relations. Applied optics, 33(18), pp.3905-3911.

10. F. Bagci, and B. Akaoglu, 2013. A 1x4 power-splitter based on photonic crystal Y-splitter and directional couplers. Opt. Pura Opt. Pura Apl, 46(3), pp.265-273.

11. T. Shirai, A. Ishikawa, Y. Matsushima, H. Ishikawa, and K. Utaka, "Analysis on Si modified MMI-waveguide-type optical switch operated with carrier injection," IEEE 22nd Microoptics Conference (MOC) (pp. 316–317), (2017).

12. Á Rosa, A. Gutiérrez, A. Brimont, A. Griol, and P. Sanchis, "High performace silicon 2 (2 optical switch based on a thermo-optically tunable multimode interference coupler and efficient electrodes," Opt. Express 24(1), 191–198 (2016).

13. B. U. Sohn, J. W. Choi, D. K. Ng, and D. T. Tan, "Optical nonlinearities in ultra-silicon-rich nitride characterized using z-scan measurements," Sci. Rep. 9(1), 1–7 (2019).

14. M. Jacques, A. Samani, E. El-Fiky, D. Patel, Z. Xing, and D. V. Plant, "Optimization of thermo-optic phase-shifter design and mitigation of thermal crosstalk on the SOI platform," Opt. Express 27(8), 10456–10471 (2019).

15. N. C. Harris, Y. Ma, J. Mower, T. Baehr-Jones, D. Englund, M. Hochberg, and C. Galland, "Efficient, compact and low loss thermo-optic phase shifter in silicon," Opt. Express 22(9), 10487–10493 (2014).

16. K. P. Lim, V. Krishnamurthy, J. F. Ying, J. Pu, and Q. Wang, "Ultrahigh index and low-loss silicon rich nitride thin film for NIR HAMR optics," IEEE Trans. Magn. 53(5), 1–7 (2017).

17. M. Cherchi, S. Ylinen, M. Harjanne, M. Kapulainen, and T. Aalto, Opt. Express 21 17814 (2013).

18. X. Jiang, H. Wu, and D. Dai, Opt. Express 26, 17680 (2018).

19. Y. Wang and D. Dai, J. Lightwave Technol. 38, 3994 (2020).

20. H. Qiu, Y. Liu, C. Luan, D. Kong, X. Guan, Y. Ding, and H. Hu, in Conference on Lasers and Electro-Optics (CLEO): Science and Innovations (Optical Society of America, 2020), paper STh4O-2.

21. S. Zhu, T. Hu, Y. Li, Z. Xu, Q. Zhong, Y. Dong, and N. Singh, in Electron Devices Technology and Manufacturing Conference (EDTM) (IEEE, 2019), pp. 228–230.

22. X. Sun, L. Zhang, Q. Zhang, and W. Zhang, Appl. Sci. 9, 4225 (2019).

23. B. Jalali and S. Fathpour, J. Lightwave Technol. 24, 4600 (2006).

24. S. Grillanda and F. Morichetti, Nat. Commun. 6, 8182 (2015).

25. A. D. Bristow, N. Rotenberg, and H. M. Van Driel, Appl. Phys. Lett. 90, 191104 (2007).

26. T. D. Bucio, C. Lacava, M. Clementi, J. Faneca, I. Skandalos, A. Baldycheva, M. Galli, K. Debnath, P. Petropoulos, and F. Gardes, IEEE J. Sel. Top. Quantum Electron. 26, 1 (2019).

27. D. Lin, X. Xu, P. Zheng, G. Hu, B. Yun, and Y. Cui, IEEE Photon. Technol. Lett. 32, 1265 (2020).

28. J. Joo, J. Park, and G. Kim, IEEE Photon. Technol. Lett. 30, 740 (2018).

29. D. T. H. Tan, K. J. A. Ooi, and D. K. T. Ng, Photon. Res. 6, B50 (2018).

30. K. J. A. Ooi, D. K. T. Ng, T. Wang, A. K. L. Chee, S. K. Ng, Q. Wang, L. K. Ang, A. M. Agarwal, L. C. Kimerling, and D. T. H. Tan, Nat. Commun. 8, 1 (2017).

31. S. Chung, M. Nakai, and H. Hashemi, Opt. Express 27, 13430 (2019).

32. P. H. Fu, C. Y. Chao, and D. W. Huang, IEEE Photon. J. 13, 1 (2020).

33. N.C. Harris, Y. Ma, J. Mower, T. Baehr-Jones, D. Englund, M. Hochberg, and C. Galland, Opt. Express 22, 10487 (2014).

34. T. Shibata, M. Okuno, T. Goh, T. Watanabe, M. Yasu, M. Itoh, M. Ishii, Y. Hibino, A. Sugita, and A. Himeno, IEEE Photon. Technol. Lett. 15, 1300 (2003).

35. E. Sahin, K. J. A. Ooi, G. F. R. Chen, D. K. T. Ng, C. E. Png, and D. T. H.Tan, Appl. Phys. Lett. 111, 121104 (2017).

36. Q. Wang, S. Wang, L. Jia, Y. Cai, W. Yue, and M. Yu, Opt. Express 29, 10509 (2021).

37. C.T. Phare, M.C. Shin, S.A. Miller, B. Stern, and M. Lipson, 2018. Silicon optical phased array with high-efficiency beam formation over 180-degree field of view. arXiv preprint arXiv:1802.04624.

Chapter 4

Integrated optics for Optical Phased Arrays

4.1 Background

When designing optical phased arrays, there are some key design aspects that need to be considered. Some include number of antenna elements, antenna spacing, phase/amplitude tuning mechanism, its corresponding efficiency and speed, steering range, beamwidth (spot size or resolution), and side-lobe suppression. In the previous chapter, we demonstrated the design and fabrication of some of the components that when integrated would allow for reaching some of the ideal performance criterion. The antennas can be arranged in one or two dimensions and in principle steer the optical beam in either direction. In the one-dimensional OPA, the waveguide antenna may be arranged very tightly in such a way that a large steering range can be achieved. We will demonstrate that using a low loss waveguide for the edge coupler can be used as a less complex implementation of an antenna array compared to that of the grating structures used for two-dimensional optical phased arrays. Their challenge mainly comes from the fabrication intensive process to achieve weak coupling strengths in order to get a large aperture size which in the case of an end-fire facet (or edge coupled waveguide) will not be the case. [1-3].

In the case of the SRN based OPA, one of the easiest ways to achieve phase tuning is using the thermo-optic effect, hence the shown phase shifter in the previous section can be implemented in doing so. However, of course due to the presence of silicon nanoclusters and the high third order nonlinearity of this material, other methods such as the electro-optic effect can also be implemented. In this case, since we are not concerned about the tuning speed of our OPA, we will simply use the thermo-optic effect to achieve steering. [4].

With a proper design in place, the next important challenge is the arrangement of the components for achieving high beam quality. We have chosen a one-dimensional OPA, so this can be a relatively straightforward task where the antenna is along the line of the phase shifters and splitters in a parallel fashion. The spacing between the antenna elements is governed by the grating lobes. An analogy to the Nyquist limit can be found here in the spatial domain which states two elements per wavelength are required to avoid aliasing (thus in order to avoid spatial aliasing, $\frac{\lambda}{2}$ spacing must be considered).

It is important to note that despite the scaling challenges, the larger the number of elements, the smaller the beamwidth. Here, we investigate a 16-element optical phased array to achieve a relatively large steering range while minimizing the scalability challenges. To better understand the challenges with designing this optical system and its operation, the mathematics of a one-dimensional optical phased array with uniform spacing, in addition to the integration challenges and our implementations are discussed in this chapter. [5,6].

4.2 Mathematics of phased arrays

In this thesis we will discuss the mathematics and basic terms used for a one-dimensional phased array. A one-dimensional phased array comprises of N antennas along a linear array. The spacing may vary but generally it is uniform. Thus, in this case we keep the spacing between each element at a uniform distance d = 775 nm or ($\frac{\lambda}{2}$). Assuming that the emission is being measured from the far field (Far-field $> \frac{2D^2}{\lambda}$, where D is the diameter of the antenna (N-1) x d for the uniform linear array) with uniform illumination across the array, the antenna's emitting electric field can be expressed in terms of two parts. [7-9]. First is the gain of each individual element of the array, called the element factor (G_E) and secondly, the array factor which is the effect that the array has

for beamforming. The element factor is the radiation pattern of a single antenna in the array, and it is defined by the geometry of that single antenna, in our case it is of a single mode waveguide. Note that the overall performance (gain) of the total array is limited by the individual antenna i.e., the main beam loses amplitude at the rate of the element factor- this is while the sidelobes on boresight have no amplitude loss.

The array factor is also calculated based on the geometry of the array. Here we assume that the array is equally spaced, and the phase and amplitude are the same. The normalized array factor can be written as the following:

$$A[\theta] = \frac{\sin\left(\frac{N\pi d}{\lambda}[\sin(\theta) - \sin(\theta_0)]\right)}{N\sin\left(\frac{\pi d}{\lambda}[\sin(\theta) - \sin(\theta_0)]\right)} \tag{1}$$

Where θ_0 is the target angle and since we know the relationship between the phase and the angle this relationship holds, $\Delta\Phi = \frac{2\pi d \sin(\theta)}{\lambda}$, where λ is the wavelength, d is the antenna spacing, thus the array factor can be re-written with that substitution:

$$AF[\theta, \Delta\Phi] = \frac{\sin\left(\frac{N\pi d}{\lambda}\left[\sin(\theta) - \frac{\Delta\Phi}{2}\right]\right)}{N\sin\left(\frac{\pi d}{\lambda}\sin(\theta) - \frac{\Delta\Phi}{2}\right)} \tag{2}$$

Here in Fig. 4.1. we plotted the normalized array factor at boresight for a uniform one-dimensional array with element spacing of $\frac{\lambda}{2}$ and antenna elements of N = 16, 32, and 64.
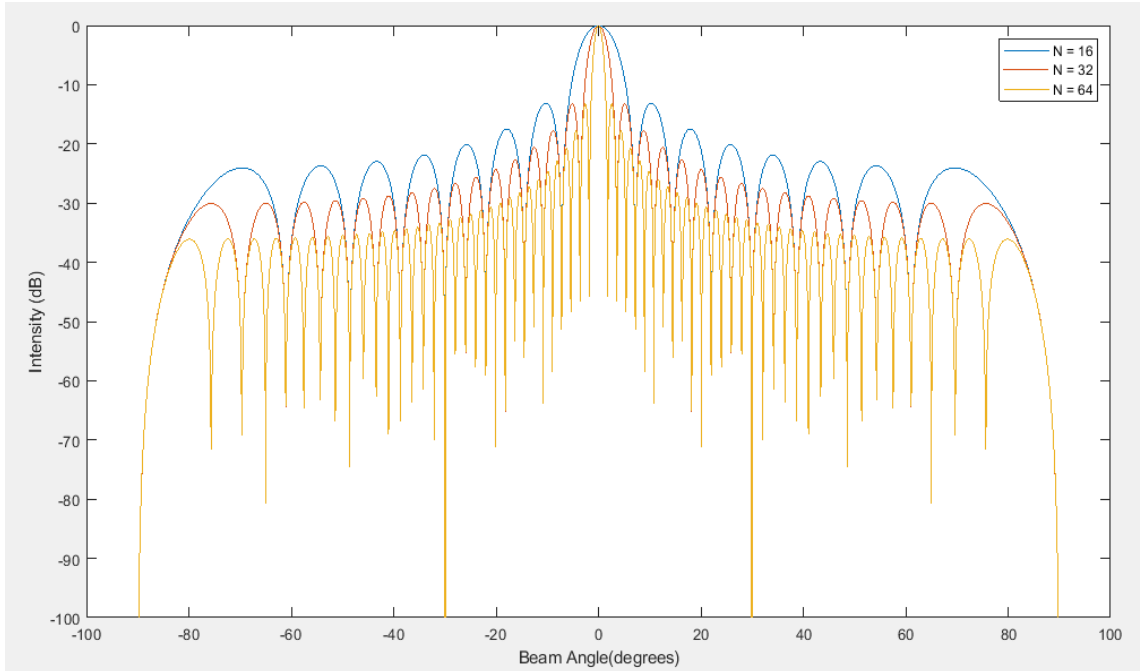
Figure 4.1. (a) The normalized far field pattern of the array factor for different number of elements at $\frac{\lambda}{2}$ spacing

We can observe that first side-lobe is at -13 dB regardless of the number of antenna elements which comes from the sinc function in the array factor. The nulls increase and the beamwidth reduces with the increase in the number of elements- see Fig. 4.2. In the case of a 16-element antenna with $\frac{\lambda}{2}$ spacing, the steering range is shown. We can also observe that the as the beam is scanned away from the boresight the beamwidth widens.
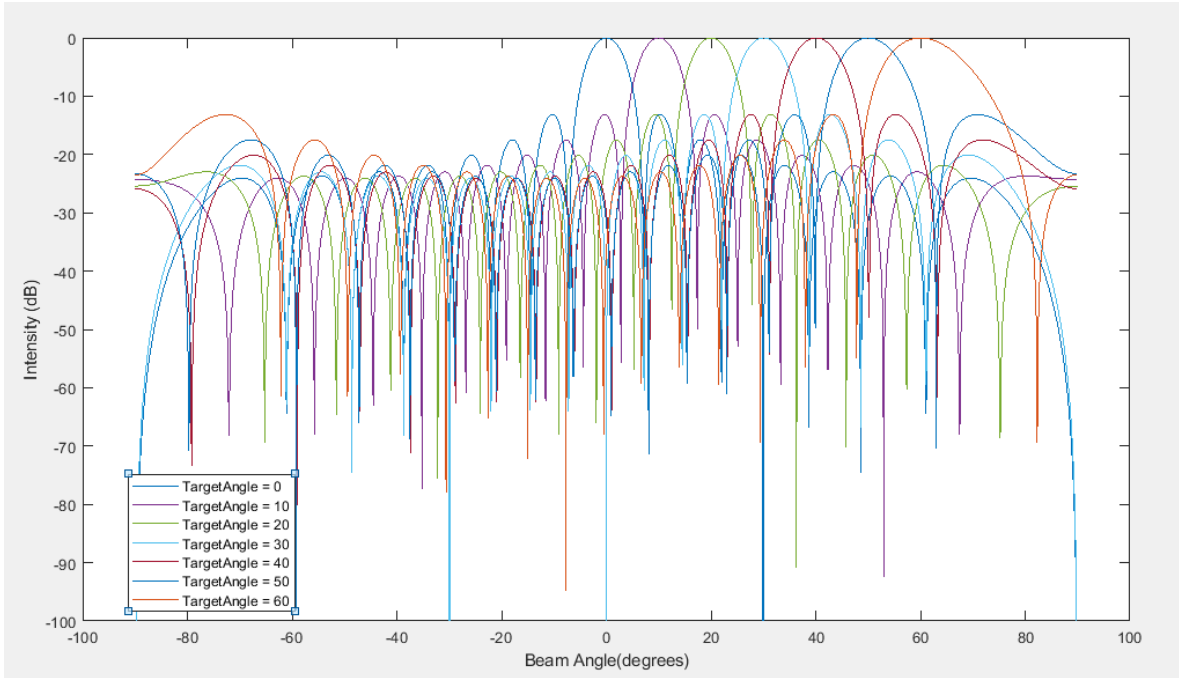
Figure 4.2. (a) The normalized transmission of a 16-elemt array factor with steering shown all the way to 60° - the doubling in beam width can be seen as the steering leads towards the theoretical limit of the phased array (before the grating lobes appear)

To better understand the angular resolution of the array, we evaluate the beamwidth and how it is a function of the steering range and the number of antenna elements. Generally, the beamwidth is measured at the fullwidth half max (or sometimes referred to as half power beam width (HPBW) of the main lobe of the antenna array. Note that since the array factor represents the electric field and not the power, we set it to $\frac{1}{\sqrt{2}}$ and not $\frac{1}{2}$.

$$\frac{1}{\sqrt{2}} = AF[\theta, \Delta\Phi] = \frac{\sin\left(\frac{N\pi d}{\lambda}\left[\sin(\theta) - \frac{\Delta\Phi}{2}\right]\right)}{16\sin\left(\frac{\pi d}{\lambda}\sin(\theta) - \frac{\Delta\Phi}{2}\right)} \tag{3}$$

Then, solving for $\Delta\Phi$, we get $\theta_{beam\ width} = 3.2^o$. The θ here is the peak at the 3-dB mark and to achieve the angular distance, we will double it so the 6.4^o. This equation can be simplified to an approximation: $\theta_B = \frac{0.886\lambda}{Nd\cos(\theta)}$. Fig. 4.3. shows the beam width for different number of elements:

53
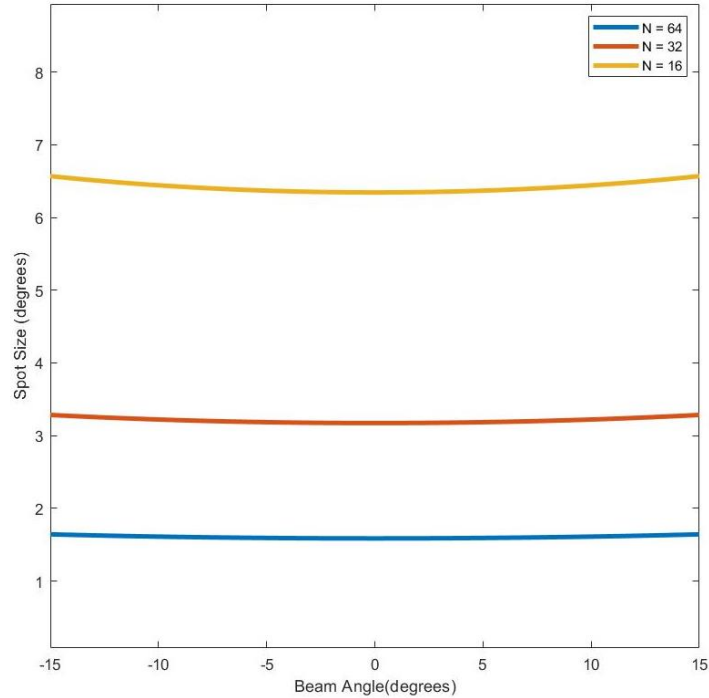
Figure 4.3. (a) The beam width also known as the spot size as a function of the beam steering for different number of antenna elements

From this plot, we can observe that the beam accuracy for a 16-element phased array, is about 6.5°. This value only holds true at boresight as it was shown in Fig. (the previous one), the beamwidth widens as it moves towards the other scanning angles. In order to keep the accuracy constant as a function of scanning angles (away from boresight), even more antenna elements are needed.

Also note that regardless of the number of antenna elements, the beamwidth doubles at ~ 60° which is primarily due to the cosine term in the denominator of the above equation which translates to a smaller cross section for the array when viewed from an angle.

In this thesis we mostly focus on the transmission side of the phased array, however so far most of the math shown here was for the array at the receiving end. Fortunately, however, antenna arrays have reciprocity and are the same for both receiving and the transmitting side.

Earlier, we discussed that our antenna design is based on $\frac{\lambda}{2}$ spacing, but the question is do we really need to keep the spacing $\leq \frac{\lambda}{2}$?

All the simulations shown so far used the element spacing of $d = \frac{\lambda}{2}$. In the plot below we see that by increasing the element spacing, in this case to 2λ, the beamwidth reduces due the decreased spacing of nulls. However, this is at the expense of grating lobes (replica of the antenna gain) appearing at larger scanning angles in this case $\pm 30^o$. This is called the spatial aliasing and can be compared to the under-sampling in analog to digital converters whereby reducing the sampling rate f_s, the frequencies above $f_s/2$ will appear as aliases in the Nyquist zone. This causes the higher order frequency terms as if they were at a lower frequency at the output.

In practice, the maximum achievable steering range is $\theta = \pm 90^o$ and for that $d = \frac{\lambda}{2}$ is required- this means no grating lobe is visible in the visible range. However, this wide range in one-dimensional antenna arrays is hard to achieve in practice which is mainly due to the limitations that the element factor and fabrication imperfections. Thus, in order to achieve the maximum angle for a given element spacing, let's start by looking at the beam angle as a function of the phase shift once again, we recall that $\Delta\Phi = \frac{2\pi d sin(\theta)}{\lambda}$, so we can rewrite

$$\theta = \arcsin\left(\frac{\Delta\Phi}{2\pi} \times \frac{\lambda}{d}\right) \tag{4}$$

This expression can only produce real solutions for arguments between -1 and +1. Since this equation has a periodic phase, we can replace the $\Delta\Phi$ with $\Delta\Phi + m \times 2\pi$, so we can re-write θ:

$$|\theta = \frac{\Delta\Phi + 2\pi \times m}{2\pi} \times \frac{\lambda}{d})|>1, m \geq 1 \tag{5}$$

To avoid the presence of grating lobes (see Fig. 4. 4.), the goal is to have only one real solution. And that is achieved only by the equation above; so, if we have solutions for $m = \pm 1$, etc. there will be nonreal solutions for θ, however if m>0 values produce real θ, then we end up with multiple solutions which are basically the grating lobes. It is important to note that at the boresight where $\Delta\Phi = 0$, there won't be a grating lobe. Some other observations from this definition can be found which is if $\frac{\lambda}{d} \geq 2$ which means $d \leq \frac{\lambda}{2}$, then you can never have multiple solutions regardless of which order m is used. Another method in avoiding these grating lobes, is to reduce the steering range i.e., minimizing $\Delta\Phi$. In literature, it has been also shown that there are other methods to overcoming the grating lobes, such as the implementation of nonuniform element spacing. [10].

Thus, in order to avoid spatial aliasing and create a clean steering with the antenna array, simply we will keep our element spacing to $\frac{\lambda}{2}$.
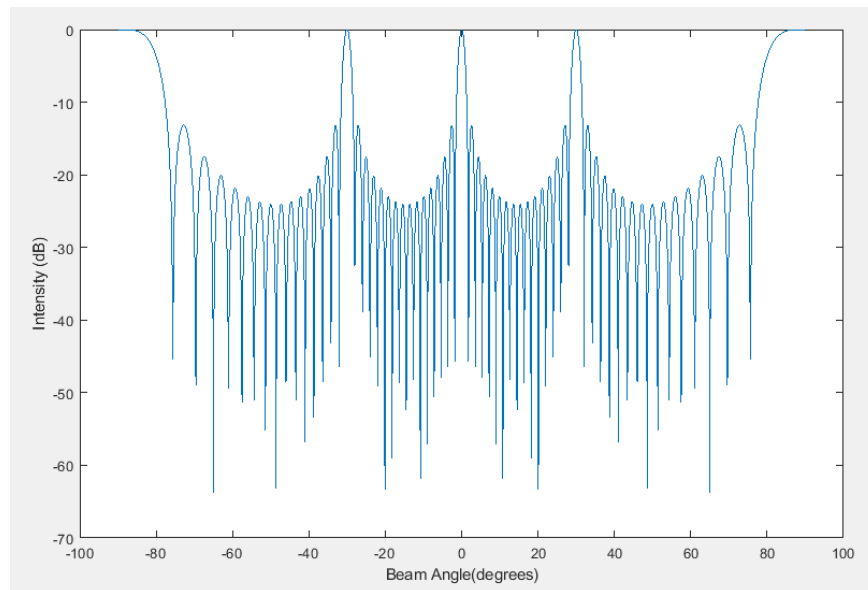
Figure 4.4. (a) The N= 16 and d = 2 λ with this increase in spacing, the beamwidth reduces at the expense of the presence of grating lobes

So far, we have seen that when no tapering is applied, the first side lobe appeared to be at 13 dB as was seen from the simulation plots. However, if in a certain application, the requirement

is to reduce the sidelobes even further, different tapering methods can simply be used to manipulate the amplitude contributions of an individual element to the overall antenna response. To apply this weighting across the array however comes with its own drawbacks i.e., the weighting will also be applied to the main lobe which could reduce the antenna gain and increase the main lobe beamwidth. Thus, we did not explore tapering options in this thesis.

4.3 Simulation of the end-fire facet SRN OPA with uniform spacing

In this section we present the results of the FDTD simulations for the end-fire facet section of the SRN OPA and observe the systematic behavior of the array factors and the element factor at a $\frac{\lambda}{2}$ spacing. In a uniform linear array with N elements, the far-field pattern depends on both the phase relationships between individual elements and their amplitude stability. The simulation (schematic shown in Fig.4.5.) incorporates realistic waveguides (later used for the experiment) of varying sizes (for phase mismatching as shown in the previous chapter) at the end fire-facet of a 16-element OPA chip. [11,12].
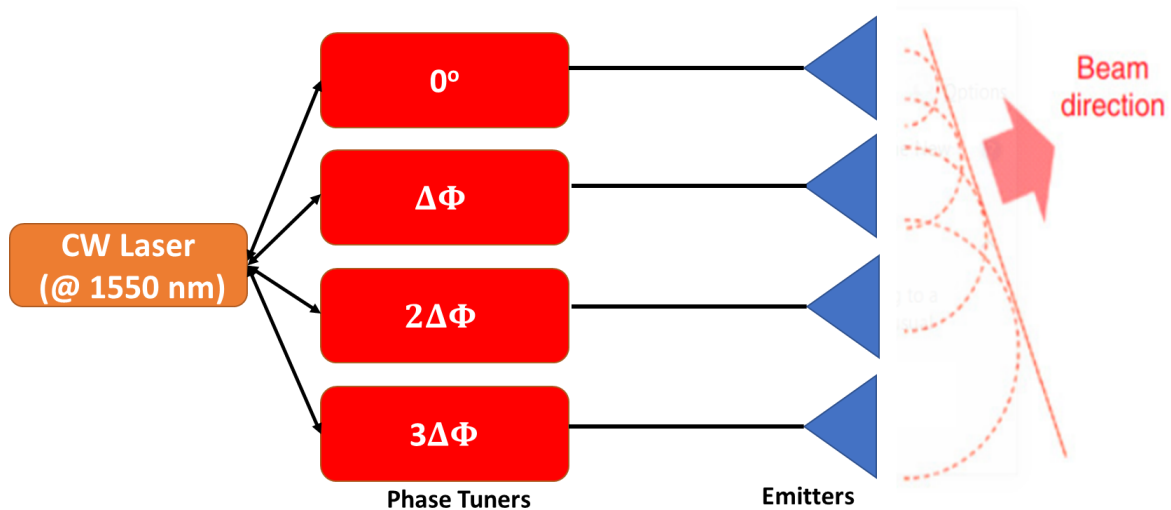
Figure 4.5. (a) The phased array schematic for the FDTD simulation where the far field beam profile is analyzed based on the different phase patterns

By varying the phase of the individual waveguiding antennas, we can observe the field intensity profile of the 16-element array for a few selected steering angles. An observation can be made that for steering angles closer to the physical limit of the array (~ 60º), the beam width increases (albeit hard to quantify in this plot), as expected.
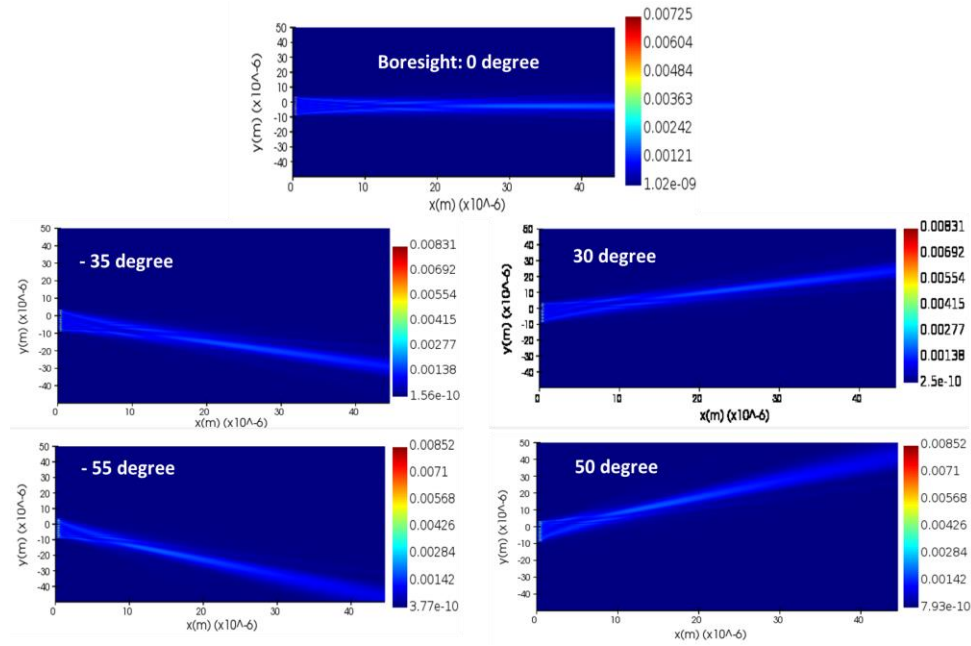
Figure 4.6. The E-field intensity profile of the steered beam at boresight, -30º,30º, -55º, and 50º

As stated, in the previous chapter, to avoid coupling between the closely spaced antenna elements, the waveguides were chosen at different widths (300, 400, and 500 nm); these values were chosen such that while creating a mismatch in the phase space, their far field element factor was similar with a uniform antenna aperture. Figure 4.6. is for the case of the nonuniform waveguide widths which we have designed.

To better understand the far field characteristics of a uniform versus nonuniform (in terms of the waveguide widths) array of antenna elements, two cases were studied. In the first case with the uniform waveguiding, all the waveguides are set to 400 nm width and 320 nm height placed at a $\frac{\lambda}{2}$ spacing (775 nm). Here the monitor was placed at a distance of 2 μm away from the sources to

58

ensure far field propagation and minimizing the presence of evanescent waves. Fig. 4.7. demonstrates the simulation environment for the waveguide antenna elements, the element factor, and the array factor. The plot on the right shows the individually normalized intensity profiles of specific target angles of the full array overlayed with the element factors of three different waveguide widths of interest, 300, 400, and 500 nm width. It can be observed in Fig 4.7. that the far field intensity profile of these three individual waveguides is very similar, and the aperture of the array is very uniform Gaussian as a result.
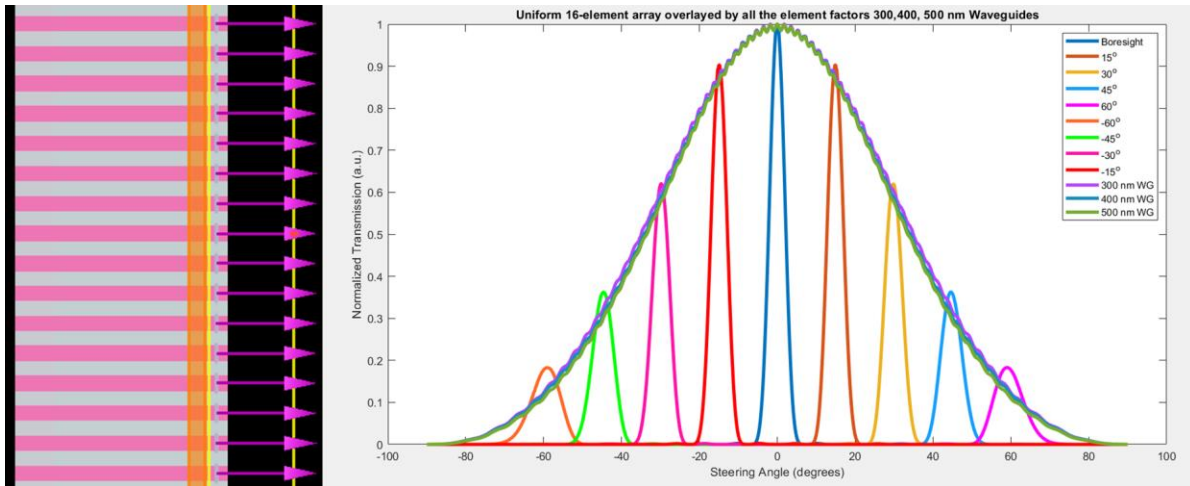
Figure 4.7. (a) (a) The schematic of the uniform array with identical waveguide widths (b) the far field pattern of individual waveguide elements (for the case where all waveguides are all either 300, 400, or 500 nm in width) overlayed with the antenna array at different steering angles

To ensure that now alternating amongst these three waveguide widths would not significantly change the performance, we repeat the simulation but with nonuniform waveguide widths. The schematic of the array is shown as well as the far field intensity profile of both the element factor and the array factor Fig. 4.8. It can be concluded that despite the negligible difference between the waveguides, the overall aperture of the array remains unchanged.

While OPA configurations can differ in terms of platforms, architecture, and components, however the key metrics for the performance evaluation or the beam forming quality, i.e., aperture (field of view) and the aliasing free steering range, solely depend on the geometrical properties of

59

the emitters. In this case, for a one-dimensional array, the analytical model can be compared to that of a multi-slit diffracted model used in Fourier Optics. [13].
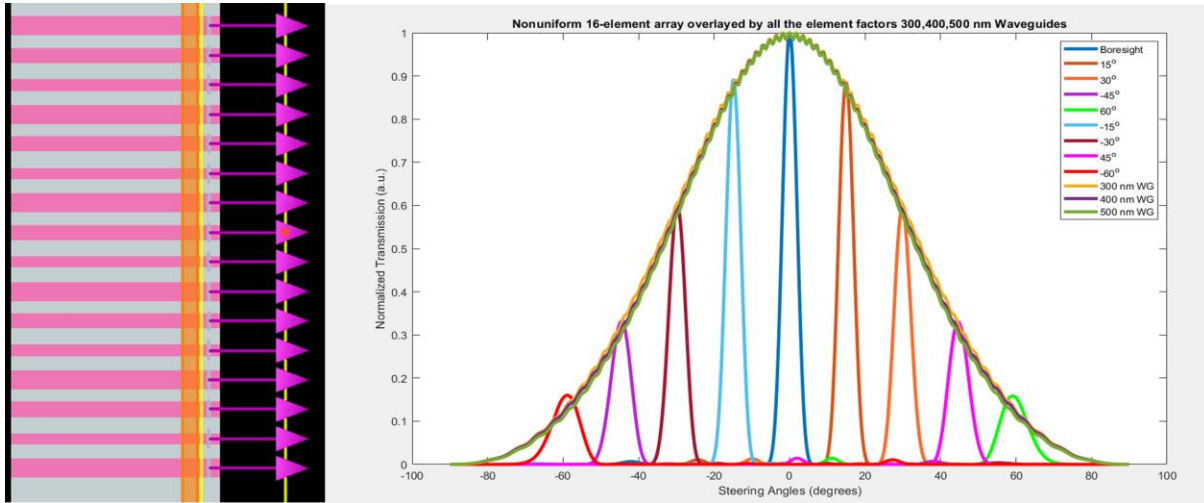
Figure 4.8. (a) (a) The schematic of the non-uniform array with similar waveguide widths (300, 400, 500 nm) (b) the far field pattern of individual waveguide elements overlayed with the antenna array at different steering angles

$$I(\theta) = I_0 \left(\frac{sin\alpha}{\alpha}\right)^2 \left[\frac{sin\left(\frac{N}{2}\right)(\delta-\phi)}{sin\left(\frac{1}{2}\right)(\delta-\phi)}\right] \tag{6}$$

$$\alpha = \frac{1}{2}kasin(\theta) \quad \delta = kdsin(\theta) \tag{7}$$

Where $I(\theta)$ represents the far field intensity of a uniformly phased array (where a uniform phase difference ϕ is applied across the array) with N antennas of size a placed at a pitch of d, I_0, i.e., the peak intensity for the element factor, $\left(\frac{sin\alpha}{\alpha}\right)^2$ is a the far field diffraction pattern of a uniformly-illuminated square array, and finally the term $(\delta - \phi)$ corresponds to the multi-slit interference pattern, and k represents the wavenumber. In our case where the grating lobes are not modulated, each lobe has a peak intensity of $N^2 I_0$. [13,14]. The above equation indicates that the far field intensity distribution of a uniform array comprises of a multi-slit interference pattern modulated by the far field diffraction pattern of the element factor i.e., the waveguide emitter.

60

4.4 The optical integration of the phased array

Now that we have demonstrated through simulation, a wide-angle beam steering for the 16-channel SRN OPA, and experimentally showed the performance of the components necessary for assembling an optical phased array, it is time to integrate the final OPA chip.
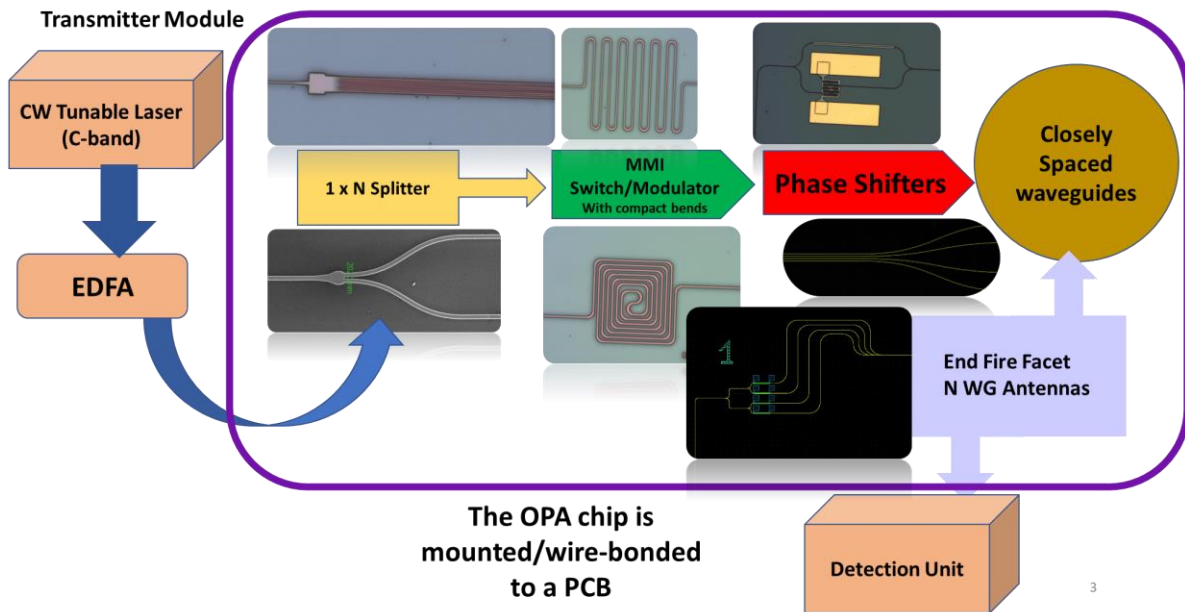
Figure 4.9. Schematic of a potential transmitter OPA chip with the necessary optical components. Here we show the optical device designs that we have fabricated and tested as potential building blocks for an OPA chip

Fig. 4.9. shows the schematic of an experimental transmitter OPA chip with the possible components that could be used to assemble it. Ideally, to divide the light on chip we will start with a series of cascaded 1x N splitters. In our design, we use 1x2 MMI splitter first and then divide each of the arms of the splitter using our 1 x 8 splitter to distribute the light into two sets of equally split sets of 8 waveguides. Each of these waveguides later continues into a 1.2 mm phase shifter with a 300 nm layer of Ni:Cr heater filament on top in a serpentine fashion covering the 65 x 65 μm^2 spiral phase shifter. These localized heaters used for the phase shifter are designed in such a way to have a highly localized thermal control at the lowest minimum thermal crosstalk. Each corresponding waveguide antenna has a phase shifter, and they are placed at a 50 μm pitch. Each

of the phase shifters is connected to a ground and a signal contact pad of size 200 x 200 μm^2 located ~ 5 mm away close to the edge of the photonic chip for further wire-bonding purposes. These contact pads are also based on Cr/Au where the chrome layer (~ 5 nm) is used for adhesion purposes and the gold layer of ~ 500-700 nm for good quality contact.

After the phase shifters, the waveguides are routed in a 90° bend to form the final end-fire facet waveguides. The layout of the overall OPA design and the OM images of the actual fabricated chip with the zoomed in MMI, phase shifter section, and the closely spaced waveguides are shown in Fig. 4.10. and Fig. 4.11. Bending radii of 15 μm all the way to 85 μm were used to minimize coupling as the waveguides are brought close to each other and to avoid a significant change in their effective index and the loss of modal shape. The 16-waveguides now brought together at $\frac{\lambda}{2}$ spacing propagate for a distance of ~ 2 mm and then terminate close to the edge of the chip and will eventually get diced and cleaned using focused ion beam (FIB). After the facets are exposed, the waveguides act as emitters following a Gaussian pattern.

While we did not use the MMI switch in this configuration for amplitude control of the waveguide antennas, it is important to note that we could replace the phase shifters with these MMI switches to achieve steering through amplitude modulation of the individual waveguide antennas. Further modifications of this chip could potentially involve a combination of both phase shifter and MMI switch to create a more uniform far field emission and or to improve with the side lobe suppression.

62
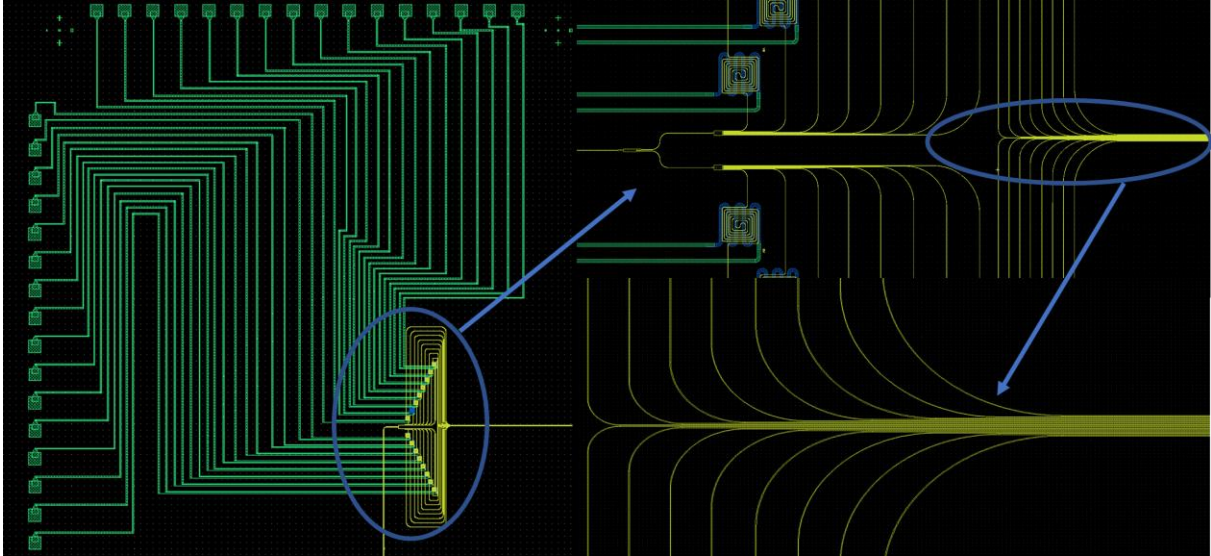
Figure 4.10. The overall layout of the photonic chip showing the contact pads and the zoomed in image of the MMI coupler, the spiral based phase shifter with serpentine heaters, and the closely spaced waveguides at the output
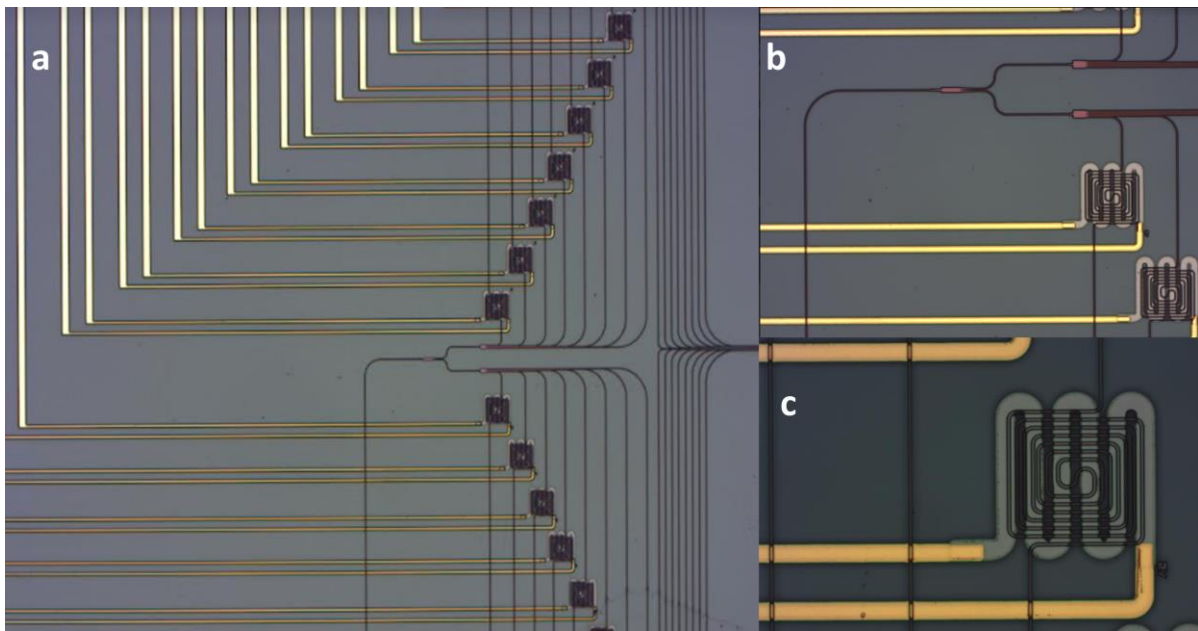
Figure 4.11. (a) The OM image of the zoomed in OPA chip (b) MMI couplers and phase shifters (c) zoomed in OM image of the phase shifter with the contact pads attached

4.5 Conclusion

To summarize, we have shown the mathematics and the theoretical models for a one dimensional optical phased array. We show the performance dependency of the overall antenna array on the antenna and element factors. We further show that the best spacing between the

elements chosen must be $\frac{\lambda}{2}$ to avoid spatial aliasing/ the presence of grating lobes. We show the performance of a 16-element phased array with the $\frac{\lambda}{2}$ spacing and demonstrate its physical limit for a steering of around $\pm$ 60 degrees along with a comparison study of the dependence of the number of elements on the spot size of the array.

Simulations for the implementation of the end-fire facet architecture was done for two cases of nonuniform (alternating waveguide widths) and uniform wave-guiding arrays.

We can conclude that far field projection of both element and array factor in both cases was very similar and hence the decision was to go with the nonuniform array design to ensure that the waveguides do not interact with each other in the phase space.

Finally, we show a full integration of all the photonic building blocks shown in chapter 3. With the earlier FDTD simulations of the array and the theoretical model, we expect to achieve wide range of steering.

Chapter 4, in part, contains materials from "Wide-angle optical beam steering in SRN" submitted for publication in Optics Letters and co-authored by Prabhav Gaur, Alex Friedman, Karl Johnson, Steve Pappert, Yeshaiahu Fainman, and Paul Yu. The dissertaion author was the first author of the manuscript.

Bibliography

Chapter 4

1. A. Yaacobi, J. Sun, M. Moresco, G. Leake, D. Coolbaugh, and M. R. Watts, "Integrated phased array for wide-angle beam steering," Opt. Lett. 39, 4575-4578 (2014)

2. Z. Li, B. Liu, C. Rui Liao, and H. Y. Fu, "Solid-state FMCW LiDAR with in-fiber beam scanner," Opt. Lett. 47, 469-472 (2022)

3. X. Cao, G. Qiu, K. Wu, C. Li, and J. Chen, "Lidar system based on lens assisted integrated beam steering," Opt. Lett. 45, 5816-5819 (2020)

4. H. Nejadriahi, A. Friedman, R. Sharma, S. Pappert, Y. Fainman, and P. Yu, "Thermo-optic properties of silicon-rich silicon nitride for on-chip applications," Opt. Express 28, 24951-24960 (2020)

5. C.V. Poulton, 2016. Integrated LIDAR with optical phased arrays in silicon photonics (Doctoral dissertation, Massachusetts Institute of Technology).

6. P. Delos, B. Broughton, and J. Kraft, 2020. Phased array antenna patterns-part 1: Linear array beam characteristics and array factor. Analog Dialogue, 54, pp.1-3.

7. P. Delos, B. Broughton, and J. Kraft, 2020. Phased array antenna patterns—part 2: grating lobes and beam squint. Anal Dialogue Anal Devices, 54(2).

8. P. Delos, B. Broughton, and J. Kraft, 2020. Phased-Array Antenna Patterns (Part 6)-Sidelobes and Tapering. 51 Choosing the Best Vibration Sensor for Wind Turbine Condition Monitoring, p.11.

9. R.C. Hansen, 2009. Phased array antennas (Vol. 213). John Wiley & Sons.

10. F.J. Pompei, and S.C. Wooh, 2002. Phased array element shapes for suppressing grating lobes. The Journal of the Acoustical Society of America, 111(5), pp.2040-2048.

11. M.R. Kossey, 2018. End-Fire Silicon Waveguides as a Platform for Optical Phased Arrays (Doctoral dissertation, Johns Hopkins University).

12. W. Xu, L. Zhou, L. Lu, and J. Chen, 2019. Aliasing-free optical phased array beam-steering with a plateau envelope. Optics express, 27(3), pp.3354-3368.

13. L. Zhang, Y. Wang, Y. Hou, J. Song, 2022. Uniform rectangular distribution of far-field intensity by optical phased array. Optics Communications, 507, p.127661.

14. W. Xu, L. Lu, L. Zhou, and J. Chen, 2017, October. Reconfiguring the 16×16 silicon optical switch for optical beam steering application. In 2017 International Topical Meeting on Microwave Photonics (MWP) (pp. 1-4). IEEE.

Chapter 5

SRN based Optical Phased Array

5.1 Background

The idea behind silicon photonics optical phased arrays is to replace the complex free-space optical systems used mainly in LiDAR technologies. To design such a system requires careful consideration in terms of many systems design specification such as the material platform, eye safety, and etc. As mentioned before the two popular material choices used in optical phased arrays are silicon and silicon nitride. However, each of these materials has their own downsides for offering an ideal platform for optical phased array/LiDAR. Silicon is mostly implemented in the silicon on insulator (SOI) wafers and silicon nitride is also commonly found in many CMOS foundries as a wave-guiding material. However, silicon can only guide above its band gap wavelength at around 1.1 μm while silicon nitride is transparent at both visible and the near infrared wavelength regions. In majority of silicon photonics processes, both silicon and silicon nitride waveguides are surrounded by cladding oxide which has an absorption band of 3.7 μm and effectively introduces the upper limit for both types of these waveguides. Usually silicon photonics phased array/ LiDAR systems work around the telecom wavelengths (O and C bands), however depending on the application of interest, this can change. [1-3].

Silicon nitride's transparency around (800 to 1100 nm) allows for leveraging many light sources, and implementation of many applications that could not be achieved otherwise using silicon. On the other hand, silicon nitride's lack of an efficient phase tuning leads to greater power consumption and larger phase shifters.

Table 5.1. A comparison of typical designs and properties between Si and SiN waveguide with SiO$_2$ cladding

	Transparency μm	Thickness μm	Loss dB/cm	Bending μm	$\frac{\beta_{TO}}{K}$	n2 cm^2/GW	β_{TPA} cm/GW
Si	1.1-3.7	0.2-0.5	1-3	5-50	1.8 x 10^{-4}	5 x 10^{-5}	0.5
SiN	0.5-3.7	0.2-2	0.2-2	20-200	2-4 x 10^{-5}	3-7 x 10^{-6}	negligible

The optical (propagation) loss values shown in Table 5.1. are good measures of scalability of the aforementioned platforms. While silicon's thermo-optic coefficient is an order of magnitude higher and allows for a relatively more efficient tuning, it is important to note waveguides for optical phased arrays often need to transmit at very high power for which the nonlinear effects are not negligible and must be taken into account. Silicon has a relatively large TPA coefficient. Generally, β_{TPA} (the TPA coefficient) and the propagation loss can be described as $10 \log_{10}(e) \frac{\beta_{TPA}}{A_{eff}}$ where the A_{eff} is the effective mode size of a typical silicon waveguide (220 x 500 nm^2) at 1550 nm. In this case the loss being around 2 dB/cm/W, TPA introduces non-negligible loss when transmitting above 100's of mW of optical power which is a bottleneck for real implementation of optical phased array and their full integration in LiDAR system. Hence, our SRN based optical phased array with a larger transparency window starting at 700 nm and negligible TPA coefficient compared to crystalline silicon and high thermo-optic coefficient and high refractive index for compact and more efficient devices. [4,5].

Previously we showed the theoretical and simulation studies done for the SRN OPA. To overcome the challenges in the existing OPAs, in this chapter we demonstrate the full implementation of the one-dimensional 16-element phased array. We discuss the fabrication of photonic circuit board (PCB) and the process of its wire-bonding to the photonic chip. Further we demonstrate the use of Digital to Analog Convertors (DACs) for heater control along with the algorithm used to optimize the phase tuning of the array. Next, we show the optical setup used in

this experiment along with the wide steering of 120º with a spot size of approximately 6º at boresight. Finally, we show close correlation between the experimental results and the theoretical modeling.

5.2 Photonic Circuit Board Design for heater control and wire bonding to the photonic chip

As mentioned in the previous chapter, the antenna waveguides act as dipole emitters. To actively control the phase associated with each antenna, we can use the heaters-based phase shifters. Each of these devices is routed to a contact pad at the edge of the chip and connect one end of the heater terminal to a low-resistance ground and the other to the signal. The contact pads are 400 µm center to center and 250 μm edge to edge distanced from one another - this large distance is to ensure that the wire-bonds can be easily placed next to one another without creating a short.

The photonic chip is first mounted on (using a nonconductive adhesive) a sacrificial (blank) die of the same height (575 μm) to help with raising the output facet away from the printed circuit board (PCB) and better expose the edge-emitting waveguides. Finally, they are mounted and then wire-bonded to the PCB. Fig. 5.1. (a & b) shows the pre- and post-epoxy covering of the wire-bonds.

Additionally, it is important to note that the right coating chemistry is necessary for providing a good contact and making sure the wire-bonds work properly. Hence in this case, we used Electroless Nickel, Immersion Palladium, Immersion Gold or (ENEPIG) to avoid challenges with the immersion gold and the corrosion of underlying nickel. The addition of palladium (Pd) layer between the nickel and gold limits the corrosion of the nickel by an overly aggressive immersion gold process. In this process lower gold thickness than the conventional electrolytic

nickel/immersion gold (ENIG), ENEPIG finish offers a more reliable process with improved

quality. [6,7].
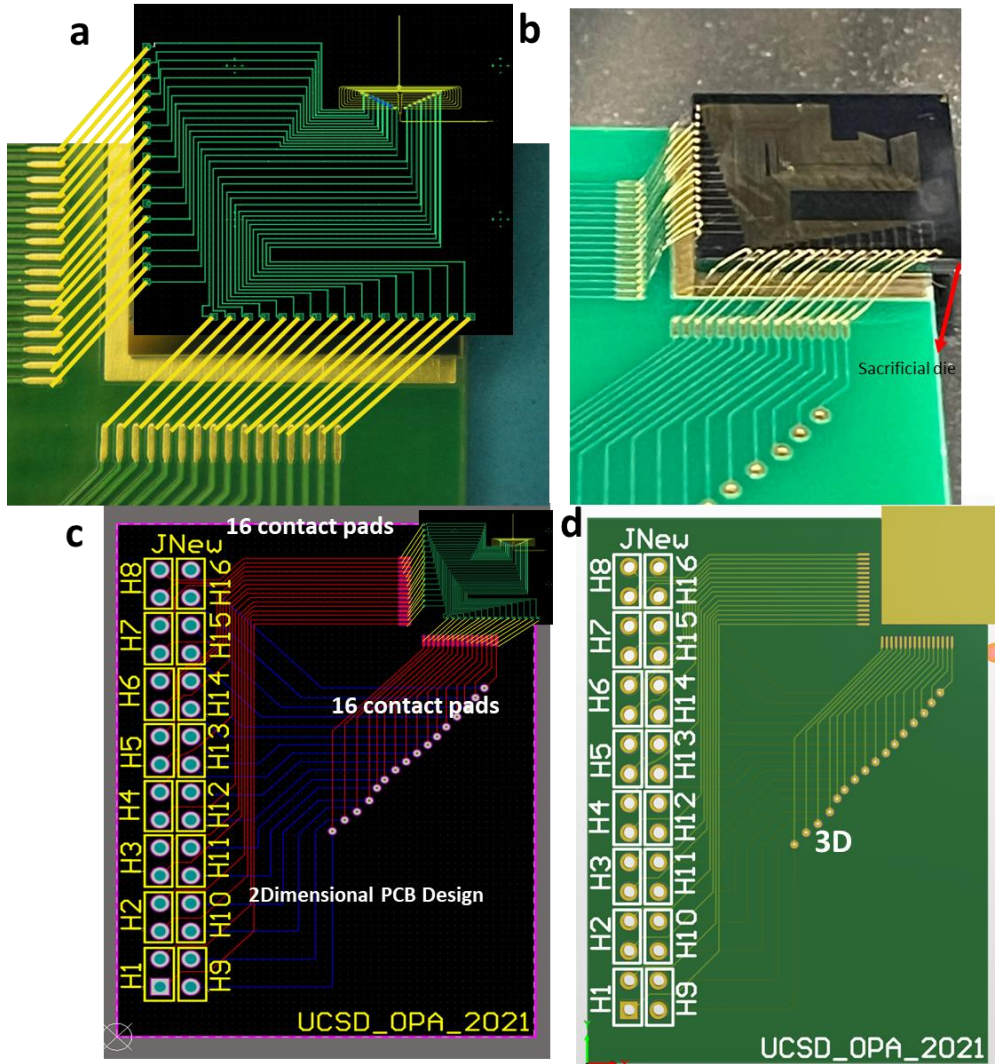
Figure 5.1. (a & b) Schematic and the OM image of the OPA chip wire-bonded to the PCB- pre adhesion process (c & d) 2D and 3D schematic of the PCB designed for wire bonding to the OPA chip with a total of 16 contact pad pairs and 32 holes for the connection of the heaters to the board

Fig. 5.1(c) shows the schematic diagram of the wire-bonded photonic chip to the designed

PCB. Fig. 5.1(d) shows the PCB design in 3D and without the photonic chip. For achieving beam

steering, the phase of light in each waveguide antenna is tuned by the applied voltages to the phase

shifters that are supplied by a PCB which is connected by the wire-bonds to the contact pads.

Our PCB was design using Altium Designer and manufactured by PCB Minion. As it can be seen there are two layers for proper routing purposes to the two sides of the chip. In our design there are 16 pads on each side of the photonic chip, and they are connected to the 32 holes on the PCB. Table 5.2. below shows the details of our PCB design:

Table 5.2. PCB Design Specifications

Length	Width	Layers	Min Trace/Space	Min Hole Size	Solder Mask	Thickness	Surface Finish	Finished Copper	Material Type
34.67 mm	45.85 mm	2	5 mil	10 mil	Green	1.6 mm	ENEPIG4	1 oz	FR4

To connect the PCB properly to an external controller (i.e., micro-controller/DAC) for voltage control, we need a proper connector. Here we use 100-mil pitch male header connectors - see Fig. 5.2. They are low cost, simple in design, and easily soldered to the board. Additionally, they can handle 1000+ mA of current which is beyond the current values that we expect in our device performance. Simple jumper wires can also be used to connect the PCB to the controllers.
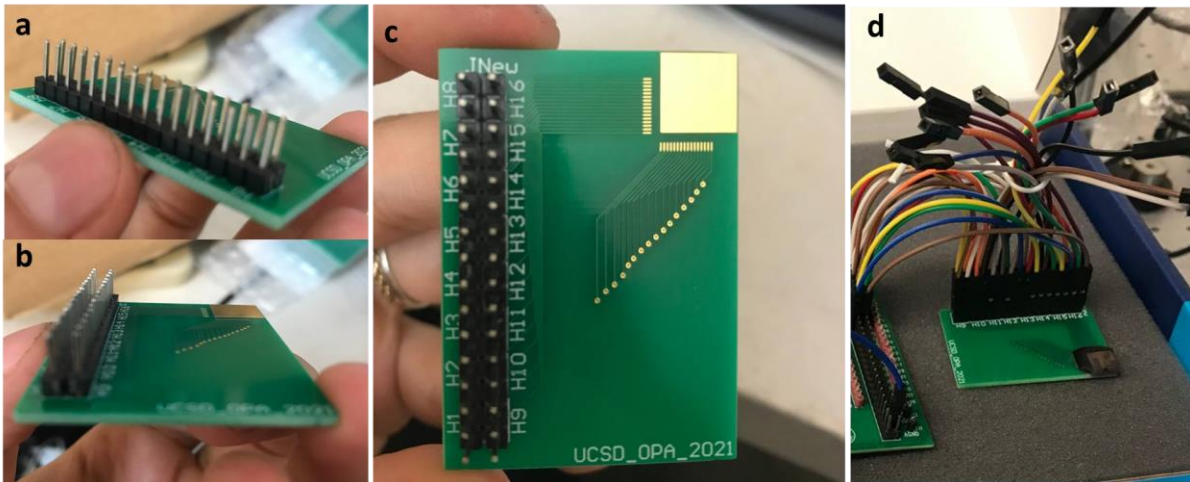

Figure 5.2. (a-c) Side and top views of the fabricated PCB with the connecter attached (d) Jumper wires connection to the PCB for further connection to the microcontroller (DAC) board

The Fig. 5.2. shows the connector placed on the PCB before the wire-bonding and after the wire-bonding process with the initial process of adding the jumper-wires for connection to the PCB.

5.3 Digital to Analog Convertor (DAC) - Gradient Descent Algorithm

The emitters in a typical OPA are controlled by a corresponding number of digital-to-analog converters. In this study, we implement the control with a 14-bit DAC consisting of 40 channels and illustrate the phase tuning by varying the voltages of the corresponding channels. The DAC used in this experiment is an evaluation board by Analog Devices which has a 12 V voltage range spanning from -4V to +8V. The least significant bit (LSB) size is simply $\frac{12V}{2^{14}} = 732.42\ \mu V$. [8,9].

To operate this evaluation board, it requires a +5V supply for Digital input source V_{cc}, in addition to the positive analog rail supply with a range of +9 to 16.5 V, for which we chose +10 V and for the negative analog rail supply we the permittable range is from -8 to -16.5 V and in this case, we chose -10 V.

In order to tune the voltages in this DAC all the values are given in a hexagonal input code and using a simple equation can be toggled back and forth given the different trigger values built in the software. Each DAC channel has several registers. In this case, the DAC's data can be written with either X1A or the X1B. Further, each of them has a gain (M) and an offset register of (C) as shown in Fig. 5.3.
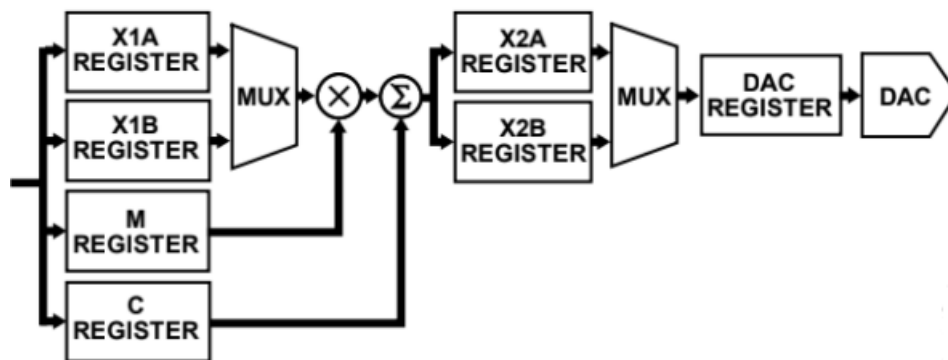

Figure 5.3. Data Registers Associated with Each DAC Channel

We use the gradient descent algorithm to find the maximum power that could be achieved for a set of phase/voltage solutions. In this algorithm, we use an iterative optimization mechanism for finding the local maxima of the power (intensity) function. In this approach, we first calculate the initial error as the difference between the current angle and the desired angle for steering (in terms of their corresponding power). Then in order to calculate the next point at which the power is maximum for the desired steering angle, we use the gradient at the current phase value, then scale it using a "learning rate" and the phase change ($\frac{\pi}{8}$) and add/subtract from the current power position shown in the IR camera; this way we create a discretized step for which we want to maximize/minimize the desired power value.

We can mathematically describe this process as:

$$P_{n+1} = P_n - \eta \nabla f(P_n)$$

Here, η refers to the learning rate which scales the gradient and controls the step size. In this case our learning rate was $\eta = \frac{\pi}{30000} \nabla f(P_n) = (phase\ (current) \pm phase\ change)$. Doing so we can extract the new set of phase values for which the power is maximum for a given a specific steering angle. This process is repeated until all the right phases and their corresponding voltage values associated for each antenna waveguide required for the range of steering angles of interests are achieved. [10,11].

In Fig. 5.4. below we show the change of area under the power curve for three iterations as a function of calculated error. As the error is increasing, the desired power value is decreasing - helping the user determine which direction the power change needs to happen in order to achieve the intended angle:

73
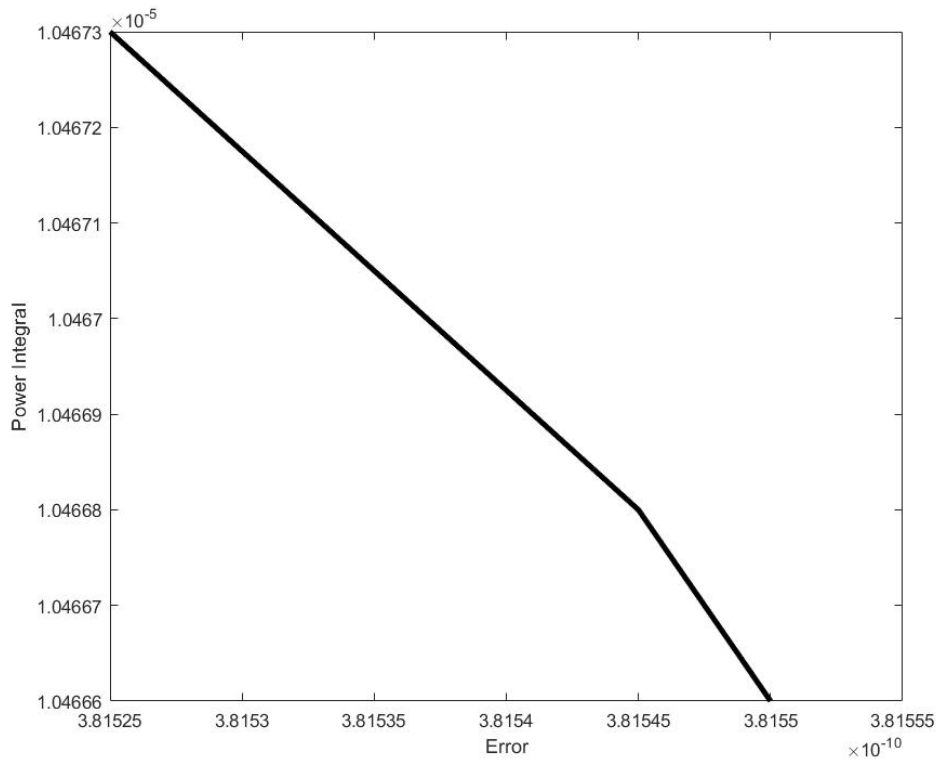
Figure 5.4. The power integral (solving for a minima) with respect to the error relation based on the gradient descent algorithm

5.4 Experimental setup, results, and verifications

Since each channel in the array is being controlled by an individual phase shifter, the DAC is used to supply and control the individual voltage

Using the optimization algorithm and the feedback from the IR camera, a set of voltage values corresponding to different steering directions are obtained and put into the DAC controller. The schematic below Fig. 5.5. shows the far-field imaging system used to do the measurements for our OPA setup.

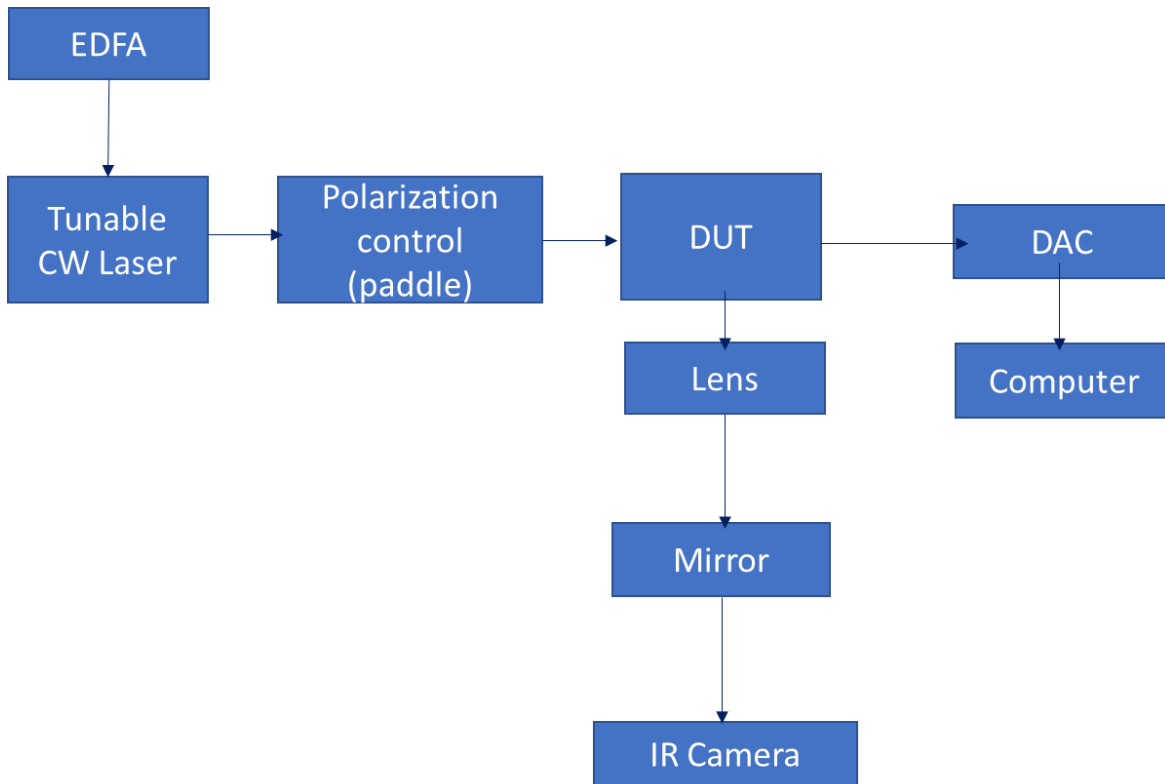Figure 5.5. The far field imaging system

After the proper phase variations/corrections were implemented using the gradient descent algorithm, we were able to achieve steering at a fixed wavelength of 1525 nm. This wavelength was chosen due to the experimentally achieved equal power values of the MMI coupler outputs with minimal phase corrections. The far field image at a few different angles is captured for three different set of phases. The Fig. 5.6. are based on a smoothened and averaged out grey scale image of the longitudinal beams. The corresponding phase values for each case is also shown. The phases of the two opposite angles are symmetric in nature, albeit in experiment can be altered according to the modifications required after fabrication imperfections. [12,13].
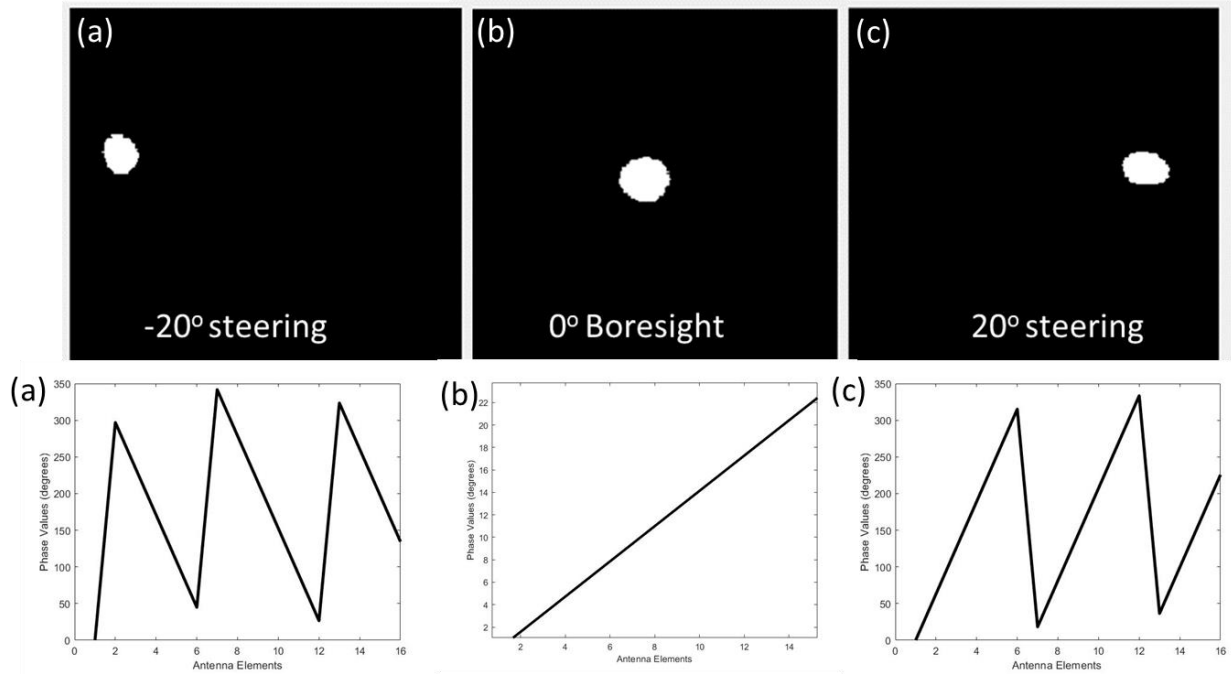
Figure 5.6. The far field images at 1525 nm after phase correction for -20°, 0°, 20° steering angles along with their corresponding phases

We experimentally achieve about 120° field of view. Fig. 5.7. is the far field beam patterns for the beam steered ±57.5° on-axis. Our array emits a high efficiency beam with 11.5 dB peak to sidelobe ratio which is very close to the theoretical limit of 13 dB ($sinc^2$ function coming from the far field pattern of a rectangular aperture). Further optimization can be done to suppress the sidelobes using different mechanisms i.e., nonuniform array spacing, etc.

Figure 5.7. (a) Measured far field optical power as a function of the steering angle over a 120° field of view, each array factor has been normalized to the power value at boresight (0°)- the element factor o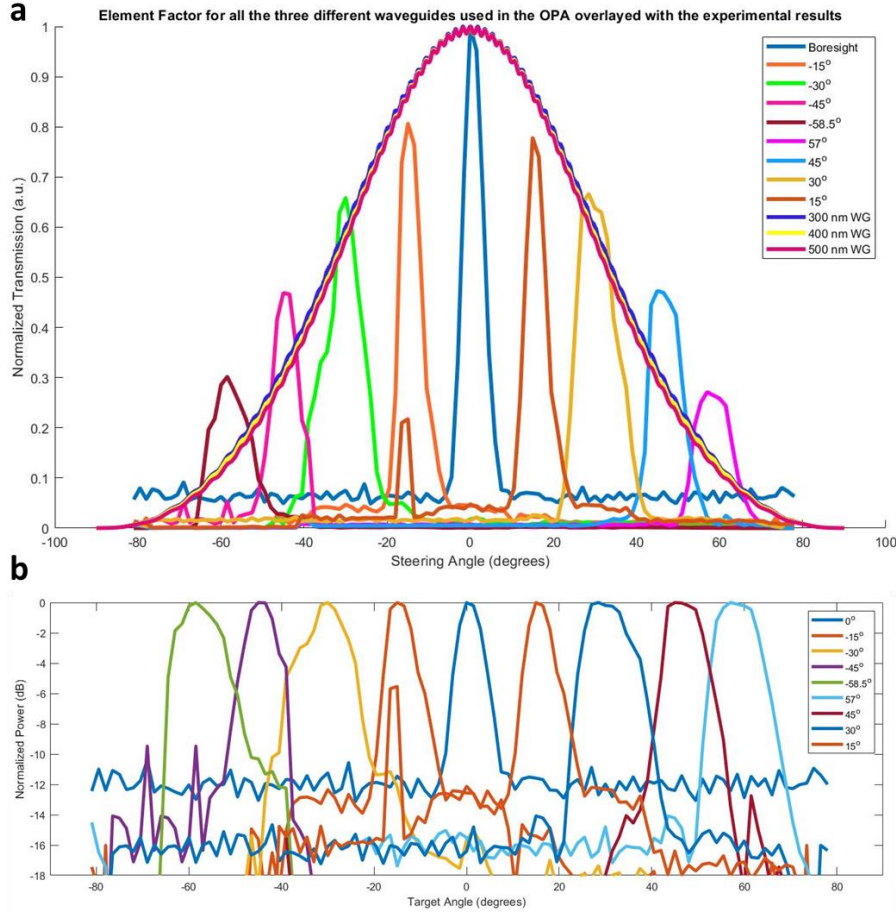f the three contributing waveguides have been overlayed on top showing the far field aperture (b) logarithmic scale plot of the beam steering normal to the array output showing peak to sidelobe ratios of 11.5 dB- the individual beams are normalized to themselves

Fig.5.7. (a) shows the measured far field normalized power versus the steering angle over a large 120° field of view for different target beam angles. Here, the power is normalized to the power at boresight (0° peak) and the amplitudes scale accordingly. Note that we have also plotted the element factor from the emission of single antenna waveguide (albeit for all the three different widths used in the antenna array i.e., 300, 400, and 500 nm) which shows close similarity to the predicted model shown in the previous chapter. In Fig.5.7. (b) we can see the logscale plot of the same, however in this case the power values are not normalized to the power value at boresight.

The spot size of the measured OPA is ~ 6.5-7° at 0° beam. Although as expected the full width half maximum of the beam widens as it goes away from the boresight and is doubled at $\pm$57.5^o. The residual sidelobes apparent in the plots above are due to the limitation in the accurate phase manipulation of the integrated phase shifters and the phase uncertainty present in each corresponding waveguiding antenna. [14,15].

5.5 Conclusions and discussions

In summary, we demonstrated that optical beam steering can be achieved in a new platform where the properties of both silicon and stoichiometric silicon nitride are combined. We used the design and fabrication of the PCB wire bonded to the photonic chip along with the gradient descent algorithm used to accurately control the phase of the array. We show approximately 120° field of view in 1D and a spot size of 6.5^o at boresight. The beam broadens at larger angles (13-14°) at approximately 60° off axis. Our component designs show high beam quality with negligible crosstalk between each phase shifters allowing for scaling to large number of antenna elements.

Chapter 5, in part, contains materials from "Wide-angle optical beam steering in SRN" submitted for publication in Optics Letters and co-authored by Prabhav Gaur, Alex Friedman, Karl Johnson, Steve Pappert, Yeshaiahu Fainman, and Paul Yu. The dissertaion author was the first author of the manuscript.

Bibliography

Chapter 5

1. S.T. Ilie, T.D. Bucio, T. Rutirawut, L. Mastronardi, I. Skandalos, H. Chong, F.Y. and Gardes, 2021, March. Silicon-rich silicon nitride CMOS platform for integrated optical phased arrays. In Smart Photonic and Optoelectronic Integrated Circuits XXIII (Vol. 11690, p. 1169005). International Society for Optics and Photonics.

2. Q. Wang, S. Wang, L. Jia, Y. Cai, W. Yue, and M. Yu, 2021. Silicon nitride assisted 1×64 optical phased array based on a SOI platform. Optics Express, 29(7), pp.10509-10517.

3. A. Marinins, S.P. Dwivedi, J.Ø. Kjellman, S. Kerman, T. David, B. Figeys, R. Jansen, D.S. Tezcan, X. Rottenberg, P. and Soussan, 2020. Silicon photonics co-integrated with silicon nitride for optical phased arrays. Japanese Journal of Applied Physics, 59(SG), p.SGGE02.

4. X. Sun, L. Zhang, Q. Zhang, and W. Zhang, 2019. Si photonics for practical LiDAR solutions. Applied Sciences, 9(20), p.4225.

5. Q. Wang, S. Wang, L. Jia, Y. Cai, W. Yue, and M. Yu, 2021. Silicon nitride assisted 1×64 optical phased array based on a SOI platform. Optics Express, 29(7), pp.10509-10517.

6. Y. Oda, M. Kiso, S. Kurosaka, A. Okada, K. Kitajima, S. Hashimoto, G. Milad, and D. Gudeczauskas, 2008, November. Study of suitable palladium and gold thickness in ENEPIG deposits for lead free soldering and gold wire bonding. In ECTC.

7. M. Ratzker, A. Pearl, M. Osterman, M. Pecht, and G. Milad, 2014. Review of capabilities of the ENEPIG surface finish. Journal of electronic materials, 43(11), pp.3885-3897.

8. AD5371, V.O.A., Evaluation Board for AD5371EBZ.

9. AD5372/AD5373 32-Channel, 16-/14-Bit,Serial Input, Voltage Output DAC.

10. S. Ruder, 2016. An overview of gradient descent optimization algorithms. arXiv preprint arXiv:1609.04747.

11. P. Baldi, 1995. Gradient descent learning algorithm overview: A general dynamical systems perspective. IEEE Transactions on neural networks, 6(1), pp.182-195.

12. H.A. Clevenson, S.J. Spector, L. Benney, M.G. Moebius, J. Brown, A. Hare, A. Huang, J. Mlynarczyk, C.V. Poulton, E. Hosseini, and M.R. Watts, 2020. Incoherent light imaging using an optical phased array. Applied Physics Letters, 116(3), p.031105.

13. J. He, T. Dong, and Y. Xu, 2020. Review of photonic integrated optical phased arrays for space optical communication. IEEE Access, 8, pp.188284-188298.

14. A. Yaacobi, J. Sun, M. Moresco, G. Leake, D. Coolbaugh, and M.R. Watts, 2014. Integrated phased array for wide-angle beam steering. Optics letters, 39(15), pp.4575-4578.

15. H. Wang, Z. Chen, C. Sun, S. Deng, X. Tang, L. Zhang, R. Jiang, W. Shi, Z. Chen, Z. Li, and A. Zhang, 2021. Broadband silicon nitride nanophotonic phased arrays for wide-angle beam steering. Optics Letters, 46(2), pp.286-289.

Chapter 6

Conclusions and Future work

In this thesis we have demonstrated that there is a clear correlation between silicon concentration of the PECVD deposited silicon nitride films and their corresponding thermo-optic coefficients. We further show that the transparency window of such high index films (> 3) expands all the way to 700 nm while retaining low optical losses ~ 3 dB/cm. We report experimental data on the thermo-optic coefficient of one of our highest index silicon rich nitride films ($n = 3.1$) achieving a value as high as $(1.65 \pm 0.08) \times 10^{-4}$ K^{-1}. This is one of the highest reported values for a PECVD deposited silicon nitride film and it is comparable to that of crystalline silicon making SRN a potential platform for photonic integrated systems.

Furthermore, once it was shown that the PECVD deposited silicon rich nitride films demonstrated to have high index contrast (with oxide), low loss, and high thermo-optic coefficient, we developed the design, fabrication, and characterization of the integrated photonics components that could be used as the building blocks to realize an OPA. These components include splitters such asy-branch coupler with 0.15 dB insertion loss, 1 x N MMI splitters (1 x8 MMI with 0.55 dB of insertion loss) to distribute the power, thermo-optic phase shifter ($P_\pi = 8 \, mW$) and switches ($P_\pi = 23 \, mW$) for phase control, and tight bends for facilitating a compact footprint. It is important to note that the uniform array was implemented for packing compactness in addition to simplicity of design. Nevertheless, to minimize the secondary (side) lobes and maximize the power in the main lobe, several approaches are proposed in literature to reduce the side lobe level (SLL). For example, amplitude windowing (apodization) has shown to reduce the SLL in arrays of element separation $\leq \frac{\lambda}{2}$. Other optimization techniques such as arranging the antenna elements according to different algorithms i.e., Fermat's spiral significantly reduces the SLL even in the

case of antenna arrays with spacing that exceeds $\frac{\lambda}{2}$ (where the presence of grating lobes is guaranteed).

Finally, we were able to demonstrate beam steering through a 1-D OPA based on a SOI platform (the high index SRN). We showed that for a 16-elements OPA, we can show 6-degree spot size at boresight and ~ 12-14 degrees at $\pm$ 60 degrees (off boresight). Additionally, we show a wide steering range from -58.5 to 57 degrees. The demonstrated experimental results have been accurately verified with the theoretical model and show close similarities.

Since the OPAs have attracted a lot of interest as a key component in the solid-state light detection and ranging (LiDAR) systems, they require a wide beam-steering performance in 2D space. So far true 2D OPAs have been demonstrated to have a limited range of steering within 10° with $9\mu m$ array pitch. Although 1D OPAs can achieve wide beam steering such as in our case, however, this is only in the transverse direction. For longitudinal beam steering, different modifications need to be employed. In addition to the thermos-optic or other means of phase tuning, wavelength tuning is needed. In this case, grating structures need to be used for which effective index variations and or the grating period are important factors to consider in order to achieve the proper steering range needed to go above the existing limits. Existing OPAs have drawbacks with respect to large scale integration and wide transversal steering due to the large power consumption, low refractive index (in case of stoichiometric silicon nitride) and the presence of nonlinear losses preventing such large-scale integrations (silicon).

As new material platforms continue to be considered for the advancement of integrated photonics, we believe, silicon rich silicon nitride, a CMOS compatible material, can offer additional capabilities and functionalities to the existing photonics portfolio.

Finally, there will be many challenges to make a fully CMOS compatible solid-state LiDAR, particularly based on an OPA. Some challenges relate to the fundamental limitations of the mechanism or materials, and some are purely engineering difficulties. We believe that silicon rich silicon nitride has addressed many of the material challenges present in the existing OPAs. Additionally, adopting silicon photonics based coherent receivers to realize Frequency Modulated Continuous Wave (FMCW) demodulation in combination with the more traditional beam steering could be the closest to an upcoming product. Another possibility could also be using SRN based OPAs for 1D steering and a more traditional steering method for other field of view (FOV) dimension, may be an easier solution to enter the market compared to the existing solutions in 2D where it could be more challenging to make into a product.